50th AIAA/ASME/ASCE/AHS/ASC Structures, Structural Dynamics, and Materials Conference
17th
4 - 7 May 2009, Palm Springs, California

AIAA 2009-2402

Nonlinear Aeroelasticity of a Very Flexible Blended-Wing-Body Aircraft

Weihua Su[1] and Carlos E. S. Cesnik[2]

Department of Aerospace Engineering
The University of Michigan, Ann Arbor, MI, 48109-2140

Blended-wing-body (BWB) aircraft with high-aspect-ratio wings is an important configuration for high-altitude long-endurance unmanned aerial vehicles (HALE UAV). Recently, Northrop Grumann created a wind tunnel model under the Air Force's High Lift over Drag Active (HiLDA) Wing program to study the aeroelastic characteristics of blended-wing-body for a potential Sensorcraft concept. This paper presents a study on the coupled aeroelastic / flight dynamics stability and response of a BWB aircraft that is modified from the HiLDA experimental model. An effective method is used to model very flexible BWB vehicles based on a low-order aeroelastic formulation that is capable of capturing the important structural nonlinear effects and couplings with the flight dynamics degrees of freedom. A nonlinear strain-based beam finite element formulation is used. Finite-state unsteady subsonic aerodynamic loads are incorporated to be coupled with all lifting surfaces, including the flexible body. Based on the proposed model, body-freedom flutter is studied, and is compared with the flutter results with all or partial rigid-body degrees of freedom constrained. The applicability of wind tunnel aeroelastic results (where the rigid-body motion is limited) is discussed in view of the free flight conditions (with all 6 rigid-body degrees of freedom). Furthermore, effects of structural and aerodynamic nonlinearities as well as wing bending/torsion rigidity coupling on the stability and gust response are also studied in this paper.

I.   Introduction

HIGH-ALTITUDE Long-Endurance (HALE) vehicles feature light wings with a high aspect ratio. These long and slender wings, by their inherent nature, can maximize lift to drag ratio. On the other hand, these wings may undergo large deformations during normal operating loads, exhibiting geometrically nonlinear behavior. Van Schoor, Zerweckh and von Flotow[1] studied aeroelastic characteristics and control of highly flexible aircraft. They used linearized modes including rigid-body modes to predict the stability of the aircraft under different flight conditions. Their results indicate that unsteady aerodynamics and flexibility of the aircraft should be considered so as to correctly model the dynamic system. Patil, Hodges, and Cesnik[2] studied the aeroelasticity and flight dynamics of HALE aircraft. The results indicate that the large wing deformations due to the high aspect-ratio structure may change the aerodynamic load distributions comparing to the initial shape. This brings significant changes to the aeroelastic and flight dynamic behaviors of the wings and overall aircraft. Therefore, the analysis results obtained through linear analysis based on the undeformed shape may not be valid in this case, since those effects can only be caught through nonlinear analysis. The vehicle should be first solved in its nonlinear steady state. Analysis can be carried out by linearizing the system about this state. Drela[3] modeled a complete flexible aircraft as an assemblage of joined nonlinear beams. In his work, the aerodynamic model was a compressible vortex/source-lattice with wind-aligned trailing vorticity and Prandtl-Glauert compressibility correction. The nonlinear equation was solved using a full Newton method. Through simplifications of the model, the computational size was reduced for iterative preliminary design. More recently, Shearer and Cesnik[4, 5] studied the nonlinear flight dynamics of very flexible aircraft. The nonlinear flight dynamic responses are governed by the coupled equations of the 6 DOF body motions and the aeroelastic equations. They also compared three sets of solution types, which are rigid body, linearized, and fully nonlinear solutions. Su and Cesnik[6] considered studied the nonlinear dynamic response of a highly flexible flying-wing configuration. An asymmetric distributed gust model was applied to the time domain simulations to

---

study the nonlinear behaviors of the flying-wing configuration under such perturbations. Bilinear torsional stiffness changes due to wrinkling of the skin were addressed as well. From these work, it can be concluded that the coupled effects between these large deflection and vehicle flexibility and flight dynamics (*e.g.*, roll controllability) as well as other aeroelastic effects (*e.g.*, gust response, flutter instability) must be properly accounted for in a nonlinear aeroelastic formulation.

In the last several years, the U.S. Air Force has been working on new platform concepts for Intelligence, Surveillance, and Reconnaissance (ISR) missions, which is called "Sensorcraft." These are large HALE aircraft, with wing span of approximately 60 m. For now, three basic platform shapes have been considered: blended-wing-body, single-wing and joined-wing configurations[7]. Among the Sensorcraft concepts, this paper will focus on the blended-wing-body configuration.

The blended-wing-body has also been proposed as a solution for commercial transport planes[8]. The advantage results from a double deck cabin that extends spanwise providing structural and aerodynamic overlap with the wing. This reduces the total wetted area of the airplane and allows a long wing span to be achieved, since the deep and stiff center body provides efficient structural wingspan.

Investigations on blended-wing-body aircraft has been performed with various focuses. Liebeck[9] discussed some challenging issues in terms of the design of blended wing body concepts, including the size and application commonality, design cruise Mach number, and flight mechanics. Mukhopadhyay[10] studied structural design of blended-wing-body fuselage with the purpose for weight reduction. In his work, he designed and analyzed different efficient structural concepts for pressurized fuselage design of blended-wing-body type flight vehicles. His results indicate that efficient design of non-cylindrical pressurized structure is vital for non-conventional vehicles. Due to penalty of structural weight, advanced geometric configurations for stress balancing and composite materials are essential. Wakayama[11, 12] used Boeing Company's Wing Multidisciplinary Optimization Design (WingMOD) code to perform blended-wing-body designs. He also identified some challenges and promises of blended-wing-body optimization[13]. Ko[14] and his co-workers performed multi-discipline design optimization of a blended-wing-body transport aircraft with distributed propulsion. In their model, a small number of large engines were replaced with a moderate number of small engines and part of the engine exhaust was ducted to exit out along the trailing edge of the wing. They also integrated the model describing the effects of this distributed propulsion concept into an MDO formulation, and exhaust designs that could increase propulsive efficiency were studied.

For the Sensorcraft applications, Beran[15] and his co-workers performed static nonlinear aeroelastic analysis of a blended-wing-body. They used a high-fidelity computational process to assess the contributions of aerodynamic nonlinearities to the transonic air loads sustained by a blended-wing-body with different static aeroelastic deflections. The structural deflections prescribed in the nonlinear analysis are obtained from linear methodology. Northrop Grumann has worked on many innovative blended-wing-body designs, and the B-2 is the more recent example of a blended-wing-body. More recently, Northrop Grumann created a wind tunnel model[16] under the Air Force's High Lift over Drag Active (HiLDA) Wing program to study the aeroelastic characteristics of blended-wing-body for a potential Sensorcraft concept. The target model used in this paper is based on the HiLDA wind tunnel model.

As pointed out in the literature (*e.g.*, Refs. 2, 4-6, 17), the coupling between the low-frequency rigid-body motions of the highly flexible vehicles and the high-aspect-ratio, low-bending-frequency wings are very important. The natural frequencies of the wings are low in such a range that the aeroelastic response of the wings could be excited by the body motions, resulting in a dynamic instability which is known as body-freedom flutter. This leads to the necessity of modeling and analysis of the structural nonlinearities of the flexible vehicle and the coupled aeroelastic behaviors, including aeroelastic stabilities and gust responses, of the wing-body system. This is the main focus of the paper.

II. Theoretical Formulation

Due to the interaction between flight dynamics and aeroelastic response, the formulation includes six rigid-body and multiple flexible degrees of freedom. The structural members are allowed fully coupled three-dimensional bending, twisting, and extensional deformations. Control surfaces are included for maneuver studies. A finite-state unsteady airloads model is integrated into the system equations. The model allows for a low-order set of nonlinear equations that can be put into state-space form to facilitate stability analysis and control design. This formulation is implemented in Matlab and makes the University of Michigan's Nonlinear Aeroelastic Simulation Toolbox (UM/NAST). An overview of the formulation implemented in NAST is described below.

A. Fundamental Description

As shown in Fig. 1, a global (inertial) frame G is defined, which is fixed on the ground. A body frame B is built in the global frame to describe the vehicle position and orientation, with B_x pointing to the right wing, B_y pointing forward, and B_z being cross product of B_x and B_y. The position and orientation, with their time derivatives of the B frame can be defined as
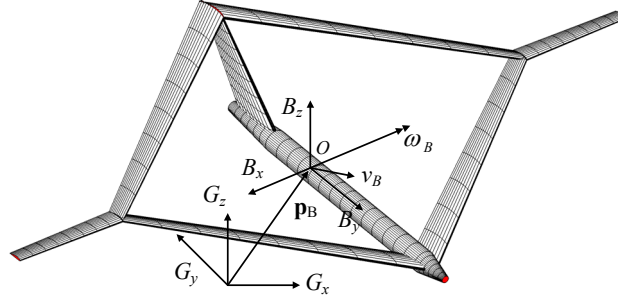

Figure 1. Global and body reference frames

$$b = \begin{bmatrix} p_B \\ \theta_B \end{bmatrix}, \qquad \dot{b} = \beta = \begin{bmatrix} \dot{p}_B \\ \dot{\theta}_B \end{bmatrix} = \begin{bmatrix} v_B \\ \omega_B \end{bmatrix}, \qquad \ddot{b} = \dot{\beta} = \begin{bmatrix} \ddot{p}_B \\ \ddot{\theta}_B \end{bmatrix} = \begin{bmatrix} \dot{v}_B \\ \dot{\omega}_B \end{bmatrix} \tag{1}$$

where p_B and θ_B are body position and orientation, both resolved in the body frame. Note that the origin of the body frame does not have to be the location of the vehicle's center of gravity.
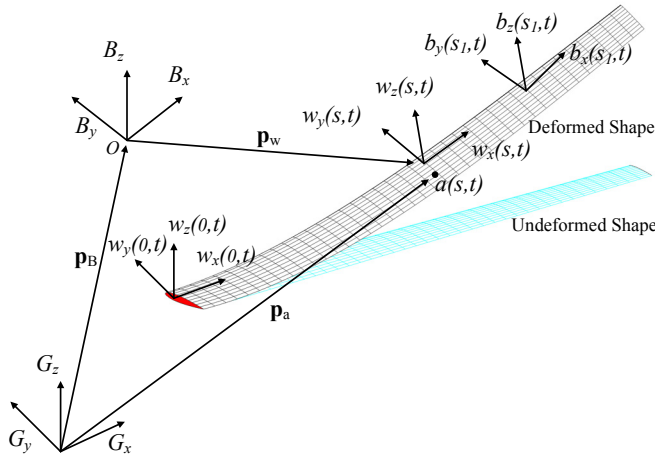

Figure 2. Flexible lifting surface frames and body (B) reference frame (for flight dynamics of the vehicle)
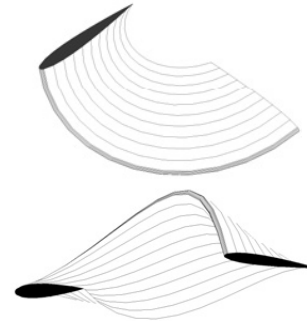

Figure 3. Deformations of a constant-strain element

As described in Fig. 2, a local beam frame (w) is built within the body frame, which is used to define the position and orientation of each node along the beam reference line. w_x, w_y, and w_z are base vectors of the beam frame, whose directions are pointing along the beam reference axis, toward the leading edge, and normal to the beam surface, respectively, resolved in the body frame.

To model the elastic deformation of slender beams, a new nonlinear beam element is developed in the work of Ref. 18. Each of the elements has three nodes and four local strain degrees of freedom, which are extension, twist, and two bending strains of the beam reference line. Figure 3 exemplifies the deformations of a constant-strain element.

Positions and orientations of each node along the beam is determined by a vector consisting of 12 components, which is denoted as

$$h(s)^T = \left[\left(p_B + p_w(s) \right)^T, \quad w_x(s)^T, \quad w_y(s)^T, \quad w_z(s)^T \right] \tag{2}$$

where, p_w is the position of w frame resolved in the body frame. In some cases, the nodal position and orientation information within the body frame is also necessary, which is

$$h_r(s)^T = \left[p_w(s)^T, \quad w_x(s)^T, \quad w_y(s)^T, \quad w_z(s)^T \right] \tag{3}$$

It is easy to see that h_r is the displacement vector due to wing deformations, while h differs h_r with the position of the body reference frame.

With the elastic and rigid body degrees of freedom defined, the complete independent variables of the strain-based formulation are as follows

$$q = \begin{bmatrix} \varepsilon \\ b \end{bmatrix} = \begin{bmatrix} \varepsilon \\ p_B \\ \theta_B \end{bmatrix}, \qquad \dot{q} = \begin{bmatrix} \dot{\varepsilon} \\ \beta \end{bmatrix} = \begin{bmatrix} \dot{\varepsilon} \\ v_B \\ \omega_B \end{bmatrix}, \qquad \ddot{q} = \begin{bmatrix} \ddot{\varepsilon} \\ \dot{\beta} \end{bmatrix} = \begin{bmatrix} \ddot{\varepsilon} \\ \dot{v}_B \\ \dot{\omega}_B \end{bmatrix} \tag{4}$$

The derivative and variation dependent variable h and h_r are related with those of the independent ones.

$$
\begin{aligned}
\delta h &= J_{h\varepsilon}\delta\varepsilon + J_{hb}\delta b & \delta h_r &= J_{h\varepsilon}\delta\varepsilon \\
dh &= J_{h\varepsilon}d\varepsilon + J_{hb}db & dh_r &= J_{h\varepsilon}d\varepsilon \\
\dot{h} &= J_{h\varepsilon}\dot{\varepsilon} + J_{hb}\dot{b} = J_{h\varepsilon}\dot{\varepsilon} + J_{hb}\beta & \dot{h}_r &= J_{h\varepsilon}\dot{\varepsilon} \\
\ddot{h} &= J_{h\varepsilon}\ddot{\varepsilon} + \dot{J}_{h\varepsilon}\dot{\varepsilon} + J_{hb}\dot{\beta} + \dot{J}_{hb}\beta & \ddot{h}_r &= J_{h\varepsilon}\ddot{\varepsilon} + \dot{J}_{h\varepsilon}\dot{\varepsilon}
\end{aligned}
\tag{5}
$$

where

$$J_{h\varepsilon} = \frac{\partial h}{\partial \varepsilon} \qquad J_{hb} = \frac{\partial h}{\partial b} \tag{6}$$

which are Jacobians obtained from kinematics[19-21].

B. Elastic Equations of Motion

The elastic equations of motion are derived by following the Principle of Virtual Work. The virtual work of a elastic wing consists of the contributions of inertia forces, internal strains and strain rates, as well as the virtual work of external loads. The corresponding inertial virtual work is derived individually. All the virtual work will need to be summed to represent the total internal virtual work of a complete vehicle.

1) Inertias

The virtual work due to the inertia of the elastic members is derived starting from the position of an arbitrary point a within the airfoil. As shown in Fig. 2, the position is given as

$$\mathbf{p}_a = \mathbf{p}_B + \mathbf{p}_w + x\mathbf{w}_x + y\mathbf{w}_y + z\mathbf{w}_z \tag{7}$$

The infinitesimal virtual work applied on a unit volume is

$$\delta W_a = \delta \mathbf{p}_a \cdot \left(-\mathbf{a}_a \rho dAds \right) \tag{8}$$

where

$$\mathbf{a}_a = \frac{d^2 \mathbf{p}_a}{dt^2} \tag{9}$$

The virtual work done by the inertia force along the beam coordinate s can be obtained by integrating Eq. (8) over each cross-section, which yields

$$\delta W^{int}(s) = -\delta h^T(s) \left\{ M(s) \begin{bmatrix} \ddot{p}_w(s) \\ \ddot{w}_x(s) \\ \ddot{w}_y(s) \\ \ddot{w}_z(s) \end{bmatrix} + M(s) \begin{bmatrix} I & \tilde{p}_w^T(s) \\ 0 & \tilde{w}_x^T(s) \\ 0 & \tilde{w}_y^T(s) \\ 0 & \tilde{w}_z^T(s) \end{bmatrix} \dot{\beta} \right.$$

$$\left. + M(s) \begin{bmatrix} \tilde{\omega}_B & 0 & 0 & 0 \\ 0 & \tilde{\omega}_B & 0 & 0 \\ 0 & 0 & \tilde{\omega}_B & 0 \\ 0 & 0 & 0 & \tilde{\omega}_B \end{bmatrix} \begin{bmatrix} I & \tilde{p}_w^T(s) \\ 0 & \tilde{w}_x^T(s) \\ 0 & \tilde{w}_y^T(s) \\ 0 & \tilde{w}_z^T(s) \end{bmatrix} \beta + 2M(s) \begin{bmatrix} 0 & \dot{\tilde{p}}_w^T(s) \\ 0 & \dot{\tilde{w}}_x^T(s) \\ 0 & \dot{\tilde{w}}_y^T(s) \\ 0 & \dot{\tilde{w}}_z^T(s) \end{bmatrix} \beta \right\} \tag{10}$$

where

$$M(s) = \int_{A(s)} \rho \begin{bmatrix} 1 & x & y & z \\ x & x^2 & xy & xz \\ y & yx & y^2 & yz \\ z & zx & zy & z^2 \end{bmatrix} dA = \begin{bmatrix} m & mr_x & mr_y & mr_z \\ mr_x & \dfrac{(I_{yy}+I_{zz}-I_{xx})}{2} & I_{xy} & I_{xz} \\ mr_y & I_{yx} & \dfrac{(I_{zz}+I_{xx}-I_{yy})}{2} & I_{yz} \\ mr_z & I_{zx} & I_{zy} & \dfrac{(I_{xx}+I_{yy}-I_{zz})}{2} \end{bmatrix} \tag{11}$$

m is the mass per unit span at each cross-section. $\begin{bmatrix} r_x & r_y & r_z \end{bmatrix}$ is the position of the center of mass of the cross-section in the w frame. I_{ij} are cross-sectional inertial properties about the reference axis (shear center in the beam cross-section). Note that the operator $(\tilde{\bullet})$ is defined for a 3x1 vector, such that

$$[\tilde{m}] \equiv \begin{bmatrix} 0 & -m_3 & m_2 \\ m_3 & 0 & -m_1 \\ -m_2 & m_1 & 0 \end{bmatrix} \tag{12}$$

In Eq. (10), $\begin{bmatrix} \ddot{p}_w(s) & \ddot{w}_x(s) & \ddot{w}_y(s) & \ddot{w}_z(s) \end{bmatrix}^T$ is the second time derivative of $h_r(s)$ in Eq (3). It can be written in terms of the second time derivative of independent variables using Eq. (5). In addition, the following relations are defined

$$J_{hb} \equiv \begin{bmatrix} I & \tilde{p}_w^T(s) \\ 0 & \tilde{w}_x^T(s) \\ 0 & \tilde{w}_y^T(s) \\ 0 & \tilde{w}_z^T(s) \end{bmatrix}, \quad \dot{J}_{hb} \equiv \begin{bmatrix} 0 & \dot{\tilde{p}}_w^T(s) \\ 0 & \dot{\tilde{w}}_x^T(s) \\ 0 & \dot{\tilde{w}}_y^T(s) \\ 0 & \dot{\tilde{w}}_z^T(s) \end{bmatrix}, \quad H_{hb} \equiv \begin{bmatrix} \tilde{\omega}_B & 0 & 0 & 0 \\ 0 & \tilde{\omega}_B & 0 & 0 \\ 0 & 0 & \tilde{\omega}_B & 0 \\ 0 & 0 & 0 & \tilde{\omega}_B \end{bmatrix} \begin{bmatrix} I & \tilde{p}_w^T(s) \\ 0 & \tilde{w}_x^T(s) \\ 0 & \tilde{w}_y^T(s) \\ 0 & \tilde{w}_z^T(s) \end{bmatrix} \tag{13}$$

With the above definitions, Eq. (10) can be simplified to

$$\delta W^{int}(s) = -\left[\delta\varepsilon^T(s) \quad \delta b^T\right]\left\{\begin{bmatrix} J_{h\varepsilon}^T M(s)J_{h\varepsilon} & J_{h\varepsilon}^T M(s)J_{hb} \\ J_{hb}^T M(s)J_{h\varepsilon} & J_{hb}^T M(s)J_{hb} \end{bmatrix}\begin{bmatrix} \ddot{\varepsilon}(s) \\ \dot{\beta} \end{bmatrix}\right.$$
$$\left. +\begin{bmatrix} J_{h\varepsilon}^T M(s)\dot{J}_{h\varepsilon} & 0 \\ J_{hb}^T M(s)\dot{J}_{h\varepsilon} & 0 \end{bmatrix}\begin{bmatrix} \dot{\varepsilon}(s) \\ \beta \end{bmatrix} +\begin{bmatrix} 0 & J_{h\varepsilon}^T M(s)H_{hb} \\ 0 & J_{hb}^T M(s)H_{hb} \end{bmatrix}\begin{bmatrix} \dot{\varepsilon}(s) \\ \beta \end{bmatrix} +\begin{bmatrix} 0 & 2J_{h\varepsilon}^T M(s)\dot{J}_{hb} \\ 0 & 2J_{hb}^T M(s)\dot{J}_{hb} \end{bmatrix}\begin{bmatrix} \dot{\varepsilon}(s) \\ \beta \end{bmatrix}\right\} \tag{14}$$

2) Internal Strain and Strain Rate
The virtual work due to the internal strain is

$$\delta W^{int}(s) = -\delta\varepsilon(s)^T k(s)\left(\varepsilon(s) - \varepsilon^0(s)\right) \tag{15}$$

where $\varepsilon^0(s)$ is the initial strain upon beam initialization.

Internal damping is added to the formulation to accurately model the actual behavior of the beams. A stiffness proportional damping is used in current formulation

$$c(s) = \alpha k(s) \tag{16}$$

Thus, the virtual work due to strain rate is

$$\delta W^{int}(s) = -\delta\varepsilon(s)^T c(s)\dot{\varepsilon}(s) \tag{17}$$

3) Internal Virtual Work on Elements
To obtain the total internal virtual on an element, one needs firstly to summate Eqs. (14), (15), and (17), and then integrate the summation over the length of each element. In practice, the integration is performed numerically.

As mentioned before, a three-node element is used in the current implementation. It is assumed that the strain over an element is constant. Some of the properties, such as inertias and displacements, are assumed to vary linearly between the nodes of an element. However, the cross-sectional stiffness $k(s)$ and damping $c(s)$ are evaluated at the middle of each element, and are assumed to be constant over the length of the elements. Using these assumptions, an element internal virtual work can be written as

$$\delta W_e^{int} = -\left[\delta\varepsilon_e^T \quad \delta b^T\right]\left\{\begin{bmatrix} J_{h\varepsilon}^T M_e J_{h\varepsilon} & J_{h\varepsilon}^T M_e J_{hb} \\ J_{hb}^T M_e J_{h\varepsilon} & J_{hb}^T M_e J_{hb} \end{bmatrix}\begin{bmatrix} \ddot{\varepsilon}_e \\ \dot{\beta} \end{bmatrix}\right.$$
$$+\begin{bmatrix} J_{h\varepsilon}^T M_e \dot{J}_{h\varepsilon} & 0 \\ J_{hb}^T M_e \dot{J}_{h\varepsilon} & 0 \end{bmatrix}\begin{bmatrix} \dot{\varepsilon}_e \\ \beta \end{bmatrix} +\begin{bmatrix} 0 & J_{h\varepsilon}^T M_e H_{hb} \\ 0 & J_{hb}^T M_e H_{hb} \end{bmatrix}\begin{bmatrix} \dot{\varepsilon}_e \\ \beta \end{bmatrix} +\begin{bmatrix} 0 & 2J_{h\varepsilon}^T M_e \dot{J}_{hb} \\ 0 & 2J_{hb}^T M_e \dot{J}_{hb} \end{bmatrix}\begin{bmatrix} \dot{\varepsilon}_e \\ \beta \end{bmatrix}$$
$$\left. +\begin{bmatrix} C_e & 0 \\ 0 & 0 \end{bmatrix}\begin{bmatrix} \dot{\varepsilon}_e \\ \beta \end{bmatrix} +\begin{bmatrix} K_e & 0 \\ 0 & 0 \end{bmatrix}\begin{bmatrix} \varepsilon_e \\ b \end{bmatrix} -\begin{bmatrix} K_e\varepsilon_e^0 \\ 0 \end{bmatrix}\right\} \tag{18}$$

where

$$K_e = k\Delta s, \quad C_e = c\Delta s, \quad M_e = \frac{1}{2}\Delta s \begin{bmatrix} \frac{1}{4}M_1 + \frac{1}{12}M_2 & \frac{1}{12}M_1 + \frac{1}{12}M_2 & 0 \\ \frac{1}{12}M_1 + \frac{1}{12}M_2 & \frac{1}{12}M_1 + \frac{1}{2}M_2 + \frac{1}{12}M_3 & \frac{1}{12}M_2 + \frac{1}{12}M_3 \\ 0 & \frac{1}{12}M_2 + \frac{1}{12}M_3 & \frac{1}{12}M_2 + \frac{1}{4}M_3 \end{bmatrix} \tag{19}$$

ε_e in the above is the elemental strain, Δs is the length of an element upon initialization, K_e is the elemental stiffness matrix, C_e is the elemental damping matrix, M_e is the elemental inertia matrix, and M_i equation are cross-sectional inertia properties at each node of an element.

4) External Virtual Work
In general, the external virtual work applied on a differential volume can be written as

$$\delta W^{ext} = \int_V \delta\mathbf{u}(x,y,z) \cdot \mathbf{f}(x,y,z) dV \tag{20}$$

where $\mathbf{f}(x,y,z)$ represents generalized forces acting on a differential volume, which may include gravity forces, external distributed forces and moments, external point forces and moments, etc. $\delta\mathbf{u}(x,y,z)$ is the corresponding virtual displacement. When beam cross-sectional properties are known, the integration of Eq. (20) over the volume is simplified as integration over the beam coordinate. The detailed derivation of the external work is listed in Refs. 19 and 21.

5) Elastic Equations of Motion
The total virtual work on the system is obtained by summation of all elements' internal and external work.

$$
\begin{aligned}
\delta W &= \sum \left(\delta W_e^{int} + \delta W_e^{ext} \right) \\
&= \begin{bmatrix} \delta\varepsilon^T & \delta b^T \end{bmatrix} \left\{ -\begin{bmatrix} J_{h\varepsilon}^T M J_{h\varepsilon} & J_{h\varepsilon}^T M J_{hb} \\ J_{hb}^T M J_{h\varepsilon} & J_{hb}^T M J_{hb} \end{bmatrix} \begin{bmatrix} \ddot{\varepsilon} \\ \dot{\beta} \end{bmatrix} \right. \\
&\quad -\begin{bmatrix} J_{h\varepsilon}^T M \dot{J}_{h\varepsilon} & 0 \\ J_{hb}^T M \dot{J}_{h\varepsilon} & 0 \end{bmatrix}\begin{bmatrix} \dot{\varepsilon} \\ \beta \end{bmatrix} -\begin{bmatrix} 0 & J_{h\varepsilon}^T M H_{hb} \\ 0 & J_{hb}^T M H_{hb} \end{bmatrix}\begin{bmatrix} \dot{\varepsilon} \\ \beta \end{bmatrix} -\begin{bmatrix} 0 & 2J_{h\varepsilon}^T M \dot{J}_{hb} \\ 0 & 2J_{hb}^T M \dot{J}_{hb} \end{bmatrix}\begin{bmatrix} \dot{\varepsilon} \\ \beta \end{bmatrix} -\begin{bmatrix} C & 0 \\ 0 & 0 \end{bmatrix}\begin{bmatrix} \dot{\varepsilon} \\ \beta \end{bmatrix} -\begin{bmatrix} K & 0 \\ 0 & 0 \end{bmatrix}\begin{bmatrix} \varepsilon \\ b \end{bmatrix} \\
&\quad \left. +\begin{bmatrix} K\varepsilon^0 \\ 0 \end{bmatrix} +\begin{bmatrix} J_{h\varepsilon}^T \\ J_{hb}^T \end{bmatrix} Ng +\begin{bmatrix} J_{p\varepsilon}^T \\ J_{pb}^T \end{bmatrix} B^F F^{dist} +\begin{bmatrix} J_{\theta\varepsilon}^T \\ J_{\theta b}^T \end{bmatrix} B^M M^{dist} +\begin{bmatrix} J_{p\varepsilon}^T \\ J_{pb}^T \end{bmatrix} F^{pt} +\begin{bmatrix} J_{\theta\varepsilon}^T \\ J_{\theta b}^T \end{bmatrix} M^{pt} \right\}
\end{aligned}
\tag{21}
$$

The equations of motion can be obtained by letting the total virtual work to be zero. Since the variation $\begin{bmatrix} \delta\varepsilon & \delta b \end{bmatrix}$ is arbitrary, the elastic system equations of motion are derived as

$$\begin{bmatrix} M_{FF} & M_{FB} \\ M_{BF} & M_{BB} \end{bmatrix}\begin{bmatrix} \ddot{\varepsilon} \\ \dot{\beta} \end{bmatrix} + \begin{bmatrix} C_{FF} & C_{FB} \\ C_{BF} & C_{BB} \end{bmatrix}\begin{bmatrix} \dot{\varepsilon} \\ \beta \end{bmatrix} + \begin{bmatrix} K_{FF} & 0 \\ 0 & 0 \end{bmatrix}\begin{bmatrix} \varepsilon \\ b \end{bmatrix} = \begin{bmatrix} R_F \\ R_B \end{bmatrix} \tag{22}$$

where the generalized inertia, damping, and stiffness are

$$M_{FF}(\varepsilon) = J_{h\varepsilon}^T M J_{h\varepsilon} \qquad\qquad M_{FB}(\varepsilon) = J_{h\varepsilon}^T M J_{hb}$$
$$M_{BF}(\varepsilon) = J_{hb}^T M J_{h\varepsilon} \qquad\qquad M_{BB}(\varepsilon) = J_{hb}^T M J_{hb}$$
$$C_{FF}(\varepsilon,\dot{\varepsilon},\beta) = C + J_{h\varepsilon}^T M \dot{J}_{h\varepsilon} \qquad C_{FB}(\varepsilon,\dot{\varepsilon},\beta) = J_{h\varepsilon}^T M H_{hb} + 2 J_{h\varepsilon}^T M \dot{J}_{hb} \qquad (23)$$
$$C_{BF}(\varepsilon,\dot{\varepsilon},\beta) = J_{hb}^T M \dot{J}_{h\varepsilon} \qquad C_{BB}(\varepsilon,\dot{\varepsilon},\beta) = J_{hb}^T M H_{hb} + 2 J_{hb}^T M \dot{J}_{hb}$$
$$K_{FF} = K$$

and the generalized force vector is

$$\begin{bmatrix} R_F \\ R_B \end{bmatrix} = \begin{bmatrix} K_{FF}\varepsilon^0 \\ 0 \end{bmatrix} + \begin{bmatrix} J_{h\varepsilon}^T \\ J_{hb}^T \end{bmatrix} N g + \begin{bmatrix} J_{p\varepsilon}^T \\ J_{pb}^T \end{bmatrix} B_F F^{dist} + \begin{bmatrix} J_{\theta\varepsilon}^T \\ J_{\theta b}^T \end{bmatrix} B_M M^{dist} + \begin{bmatrix} J_{p\varepsilon}^T \\ J_{pb}^T \end{bmatrix} F^{pt} + \begin{bmatrix} J_{\theta\varepsilon}^T \\ J_{\theta b}^T \end{bmatrix} M^{pt} \qquad (24)$$

which involves the effects from initial strains (ε^0), gravity fields (g), distributed forces (F^{dist}), distributed moments (M^{dist}), point forces (F^{pt}), and point moments (M^{pt}). The aerodynamic forces and moments are considered as distributed loads.

C. Kinematics
As discussed in Ref. 18, the governing equation, which relates the dependent displacements to the independent strains, is

$$\frac{\partial h(s)}{\partial s} = A(s)h(s) \qquad (25)$$

with $A(s)$ being a matrix function of the strains

$$A(s) = \begin{bmatrix} 0 & 1+\varepsilon_x(s) & 0 & 0 \\ \hline 0 & 0 & \kappa_z(s) & -\kappa_y(s) \\ \hline 0 & -\kappa_z(s) & 0 & \kappa_x(s) \\ \hline 0 & \kappa_y(s) & -\kappa_x(s) & 0 \end{bmatrix} \qquad (26)$$

where the blocks are all 3x3 diagonal matrices. The solution of Eq. (25) is given by Eq. (27), with the assumption that the element has a constant strain state

$$h(s) = e^{As} h_0 = e^{G(s)} h_0 \qquad (27)$$

where h_0 is the displacement of fixed or prescribed root node of the beam (boundary conditions).

The member kinematics, which is used for recovering the displacements of each node from the strain vector, is obtained by marching from the boundary node to the tips of each beam member, and solving the following equation

$$\bar{A}(\varepsilon)h = h^* \qquad (28)$$

where h is the column vector consisting of nodal positions and orientations of all nodes in the member, and h^* is a column vector consisting of boundary condition. Refs. 18 and 22 give a detail introduction of the kinematics, which consider the flexibility from both the fuselage and the wings.

D. Unsteady Aerodynamics
The distributed loads, F^{dist} and M^{dist} in Eq. (24), are divided into aerodynamic loads and user supplied loads. The aerodynamic loads used in current work are based on the 2-D finite inflow theory, provided by Ref. 23. The theory calculates aerodynamic loads on a thin airfoil section undergoing large motions in an incompressible

subsonic flow. Based known aerodynamic coefficients, the lift, moment, and drag applied on a thin 2-D airfoil section about the mid-chord are given by

$$l_{mc} = \pi\rho b^2 \left(-\ddot{z} + \dot{y}\dot{\alpha} - d\ddot{\alpha}\right) + 2\pi\rho b\dot{y}^2 \left[-\frac{\dot{z}}{\dot{y}} + \left(\frac{1}{2}b - d\right)\frac{\dot{\alpha}}{\dot{y}} - \frac{\lambda_0}{\dot{y}}\right] + 2\pi\rho bc_1\dot{y}^2\delta$$

$$m_{mc} = 2\pi\rho b^2 \left(-\frac{1}{2}\dot{y}\dot{z} - \frac{1}{2}d\dot{y}\dot{\alpha} - \frac{1}{2}\dot{y}\lambda_0 - \frac{1}{16}b^2\ddot{\alpha}\right) + 2\pi\rho b^2 c_4\dot{y}^2\delta \tag{29}$$

$$d_{mc} = -2\pi\rho b\left(\dot{z}^2 + d^2\dot{\alpha}^2 + \lambda_0^2 + 2d\dot{\alpha}\dot{z} + 2\lambda_0\dot{z} + 2d\dot{\alpha}\lambda_0\right)$$
$$-2\pi\rho b\left[c_1\dot{y}\dot{z}\delta + \left(dc_1 + bg_2\right)\dot{y}\dot{\alpha}\delta + c_1\dot{y}\lambda_0\delta + \frac{1}{2}bg_2\ddot{z}\delta + \left(\frac{1}{2}bdg_2 - \frac{1}{4}b^2g_3\right)\ddot{\alpha}\delta\right]$$

where δ is the trailing-edge flap deflection angle, b is the semichord, d is the distance of the mid-chord in front of the reference axis. $-\dot{z}/\dot{y}$ is the angle of attack that consists of the contribution from both the steady state angle of attack and the unsteady plunging motion of the airfoil. The coefficients c_i through g_i are based upon geometry and complete details are provided in Refs. 19 and 23. Finite span corrections are also included in the force distribution and come from a CFD solution of the problem. λ_0 is the inflow parameter, accounting for induced flow due to free vorticity, which is the summation of the inflow states λ as described in Ref. 23 and given by

$$\dot{\lambda} = F_1\ddot{q} + F_2\dot{q} + F_3\lambda = F_1\begin{bmatrix}\ddot{\varepsilon}\\\dot{\beta}\end{bmatrix} + F_2\begin{bmatrix}\dot{\varepsilon}\\\beta\end{bmatrix} + F_3\lambda \tag{30}$$

The different velocity components are shown in Fig. 4.
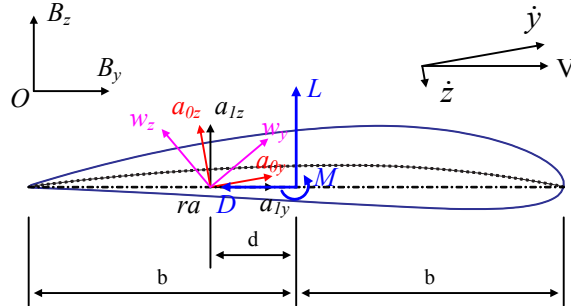
Figure 4. Airfoil coordinate system and velocity components

To transfer the loads from the mid-chord (as defined above) to the wing reference axis one may use

$$\begin{aligned}l_{ra} &= l_{mc}\\m_{ra} &= m_{mc} + dl_{mc}\\d_{ra} &= d_{mc}\end{aligned} \tag{31}$$

Furthermore, the loads are rotated to the body reference frame, which yields

$$F^{aero} = C^{Ba_l}\begin{bmatrix}0\\d_{ra}\\l_{ra}\end{bmatrix}, \qquad M^{aero} = C^{Ba_l}\begin{bmatrix}m_{ra}\\0\\0\end{bmatrix} \tag{32}$$

where C^{Ba_l} is the transformation matrix from the local aerodynamic frame to body frame.

E. Coupled Nonlinear Aeroelastic and Flight Dynamic System Equations of Motion

The coupled nonlinear aeroelastic and flight dynamic system equations of motion are obtained by augmenting the equations of rigid body motion and elastic deformations with the inflow equations, which can be represented as Eq. (33) [4, 20].

$$
\begin{bmatrix} M_{FF}(\varepsilon) & M_{FB}(\varepsilon) \\ M_{BF}(\varepsilon) & M_{BB}(\varepsilon) \end{bmatrix} \begin{bmatrix} \ddot{\varepsilon} \\ \dot{\beta} \end{bmatrix} + \begin{bmatrix} C_{FF}(\dot{\varepsilon},\varepsilon,\beta) & C_{FB}(\dot{\varepsilon},\varepsilon,\beta) \\ C_{BF}(\dot{\varepsilon},\varepsilon,\beta) & C_{BB}(\dot{\varepsilon},\varepsilon,\beta) \end{bmatrix} \begin{bmatrix} \dot{\varepsilon} \\ \beta \end{bmatrix} + \begin{bmatrix} K_{FF} & 0 \\ 0 & 0 \end{bmatrix} \begin{bmatrix} \varepsilon \\ b \end{bmatrix} = \begin{bmatrix} R_F(\ddot{\varepsilon},\dot{\varepsilon},\varepsilon,\dot{\beta},\beta,\lambda,\zeta) \\ R_B(\ddot{\varepsilon},\dot{\varepsilon},\varepsilon,\dot{\beta},\beta,\lambda,\zeta) \end{bmatrix}
$$

$$
\dot{\zeta} = -\frac{1}{2}\Omega_\zeta(\beta)\zeta \tag{33}
$$

$$
\dot{P}_B = \begin{bmatrix} C^{GB}(\zeta) & 0 \end{bmatrix}\beta
$$

$$
\dot{\lambda} = F_1 \begin{bmatrix} \ddot{\varepsilon} \\ \dot{\beta} \end{bmatrix} + F_2 \begin{bmatrix} \dot{\varepsilon} \\ \beta \end{bmatrix} + F_3 \lambda
$$

F. Linearization of the Nonlinear System Equations of Motion

The coupled nonlinear aeroelastic and flight dynamic system equations of motion are given as Eq. (33). Note that the terms of control surface deflection angles in the aerodynamic load formulations are not included, since the current target is to build a formulation for stability analysis, without considering the effects of control surfaces. The load vector that is considered here consists of aero dynamic and gravity loads only.

$$
\begin{bmatrix} R_F(\ddot{\varepsilon},\dot{\varepsilon},\varepsilon,\dot{\beta},\beta,\lambda,\zeta) \\ R_B(\ddot{\varepsilon},\dot{\varepsilon},\varepsilon,\dot{\beta},\beta,\lambda,\zeta) \end{bmatrix} = \begin{bmatrix} R_F^{aero}(\ddot{\varepsilon},\dot{\varepsilon},\varepsilon,\dot{\beta},\beta,\lambda) \\ R_B^{aero}(\ddot{\varepsilon},\dot{\varepsilon},\varepsilon,\dot{\beta},\beta,\lambda) \end{bmatrix} + \begin{bmatrix} R_F^{grav}(\zeta) \\ R_B^{grav}(\zeta) \end{bmatrix} \tag{34}
$$

and

$$
\begin{bmatrix} R_F^{aero} \\ R_B^{aero} \end{bmatrix} = \begin{bmatrix} J_{p\varepsilon}^T \\ J_{pb}^T \end{bmatrix} B_F F^{aero} + \begin{bmatrix} J_{\theta\varepsilon}^T \\ J_{\theta b}^T \end{bmatrix} B_M M^{aero} \tag{35}
$$

where R_F^{aero} and R_B^{aero} are the flexible and rigid body components of generalized aerodynamic loads, respectively. F^{aero} and M^{aero} are nodal aerodynamic loads. R_F^{grav} and R_B^{grav} are the flexible and rigid body components of generalized gravity force, respectively. The gravity force is transferred from the global frame (G) to the body frame (B). The rotation matrix between the two frames (C^{GB}) is a function of quaternions (ζ), according to Eq. (33).

Linearization is performed about a nonlinear steady state, x_0 ($\begin{bmatrix} \ddot{\varepsilon}_0, \dot{\varepsilon}_0, \varepsilon_0, \dot{\beta}_0, \beta_0, \lambda_0, \zeta_0, P_{B0} \end{bmatrix}$). Followed with some algebra work (see Ref. 21), the linearized system equations are derived as Eq. (36)

$$
M_{FF}\ddot{\varepsilon} + M_{FB}\dot{\beta} + \left(C_{FF} + C_{FF/\dot{\varepsilon}_0}\dot{\varepsilon}_0 + C_{FB/\dot{\varepsilon}_0}\beta_0\right)\dot{\varepsilon} + \left(C_{FB} + C_{FF/\beta_0}\dot{\varepsilon}_0 + C_{FB/\beta_0}\beta_0\right)\beta + K_{FF}\varepsilon
$$

$$
= R_{F/\ddot{\varepsilon}_0}^{aero}\ddot{\varepsilon} + R_{F/\dot{\varepsilon}_0}^{aero}\dot{\varepsilon} + R_{F/\varepsilon_0}^{aero}\varepsilon + R_{F/\dot{\beta}_0}^{aero}\dot{\beta} + R_{F/\beta_0}^{aero}\beta + R_{F/\lambda_0}^{aero}\lambda + R_{F/\zeta_0}^{grav}\zeta
$$

$$
M_{BF}\ddot{\varepsilon} + M_{BB}\dot{\beta} + \left(C_{BF} + C_{BF/\dot{\varepsilon}_0}\dot{\varepsilon}_0 + C_{BB/\dot{\varepsilon}_0}\beta_0\right)\dot{\varepsilon} + \left(C_{BB} + C_{BF/\beta_0}\dot{\varepsilon}_0 + C_{BB/\beta_0}\beta_0\right)\beta \tag{36}
$$

$$
= R_{B/\ddot{\varepsilon}_0}^{aero}\ddot{\varepsilon} + R_{B/\dot{\varepsilon}_0}^{aero}\dot{\varepsilon} + R_{B/\varepsilon_0}^{aero}\varepsilon + R_{B/\dot{\beta}_0}^{aero}\dot{\beta} + R_{B/\beta_0}^{aero}\beta + R_{B/\lambda_0}^{aero}\lambda + R_{B/\zeta_0}^{grav}\zeta
$$

$$
\dot{\zeta} = -\frac{1}{2}\Omega_\zeta\zeta - \frac{1}{2}\left(\Omega_{\zeta/\beta_0}\beta\right)\zeta_0
$$

$$
\dot{P}_B = \begin{bmatrix} C^{GB} & 0 \end{bmatrix}\beta + \begin{bmatrix} \left(C_{/\zeta_0}^{GB}\zeta\right) & 0 \end{bmatrix}\beta_0
$$

$$
\dot{\lambda} = F_1 \begin{bmatrix} \ddot{\varepsilon} \\ \dot{\beta} \end{bmatrix} + F_2 \begin{bmatrix} \dot{\varepsilon} \\ \beta \end{bmatrix} + F_3 \lambda
$$

where $(\bullet)_{/z_0}$ denotes $\left.\dfrac{d(\bullet)}{dz}\right|_{z_0}$ or $\left.\dfrac{\partial(\bullet)}{\partial z}\right|_{z_0}$ for different variables.

To obtain the state-space form equations, the terms on the right hand side of Eq. (36) are moved to the left, and the terms with the same variables are grouped together, which becomes

$$\left(M_{FF} - R_{F/\ddot{\varepsilon}_0}^{aero}\right)\ddot{\varepsilon} + \left(M_{FB} - R_{F/\dot{\beta}_0}^{aero}\right)\dot{\beta} + \left(C_{FF} + C_{FF/\dot{\varepsilon}_0}\dot{\varepsilon}_0 + C_{FB/\dot{\varepsilon}_0}\beta_0 - R_{F/\dot{\varepsilon}_0}^{aero}\right)\dot{\varepsilon}$$

$$+\left(C_{FB} + C_{FF/\beta_0}\dot{\varepsilon}_0 + C_{FB/\beta_0}\beta_0 - R_{F/\beta_0}^{aero}\right)\beta + \left(K_{FF} - R_{F/\varepsilon_0}^{aero}\right)\varepsilon - R_{F/\lambda_0}^{aero}\lambda - R_{F/\zeta_0}^{grav}\zeta = 0$$

$$\left(M_{BF} - R_{B/\ddot{\varepsilon}_0}^{aero}\right)\ddot{\varepsilon} + \left(M_{BB} - R_{B/\dot{\beta}_0}^{aero}\right)\dot{\beta} + \left(C_{BF} + C_{BF/\dot{\varepsilon}_0}\dot{\varepsilon}_0 + C_{BB/\dot{\varepsilon}_0}\beta_0 - R_{B/\dot{\varepsilon}_0}^{aero}\right)\dot{\varepsilon}$$

$$+\left(C_{BB} + C_{BF/\beta_0}\dot{\varepsilon}_0 + C_{BB/\beta_0}\beta_0 - R_{B/\beta_0}^{aero}\right)\beta - R_{B/\lambda_0}^{aero}\lambda - R_{B/\zeta_0}^{grav}\zeta = 0 \qquad (37)$$

$$\dot{\zeta} + \frac{1}{2}\Omega_\zeta\zeta + \frac{1}{2}\left(\Omega_{\zeta/\beta_0}\beta\right)\zeta_0 = 0$$

$$\dot{P}_B - \begin{bmatrix} C^{GB} & 0 \end{bmatrix}\beta - \left[\left(C_{/\zeta_0}^{GB}\zeta\right) \quad 0\right]\beta_0 = 0$$

$$\dot{\lambda} - F_1\begin{bmatrix}\ddot{\varepsilon}\\\dot{\beta}\end{bmatrix} - F_2\begin{bmatrix}\dot{\varepsilon}\\\beta\end{bmatrix} - F_3\lambda = 0$$

According to Eq. (35), the derivatives of the generalized aerodynamic loads can be expanded, which are given in Eq. (38). Again, one should note that all the derivatives and matrices are evaluated at the state of x_0, and the notation is omitted from the equations from now on for simplicity.

$$\frac{\partial R_F^{aero}}{\partial\ddot{\varepsilon}} = J_{p\varepsilon}^T B_F \frac{\partial F^{aero}}{\partial\ddot{\varepsilon}} + J_{\theta\varepsilon}^T B_M \frac{\partial M^{aero}}{\partial\ddot{\varepsilon}}, \quad \frac{\partial R_F^{aero}}{\partial\dot{\beta}} = J_{p\varepsilon}^T B_F \frac{\partial F^{aero}}{\partial\dot{\beta}} + J_{\theta\varepsilon}^T B_M \frac{\partial M^{aero}}{\partial\dot{\beta}}$$

$$\frac{\partial R_F^{aero}}{\partial\dot{\varepsilon}} = J_{p\varepsilon}^T B_F \frac{\partial F^{aero}}{\partial\dot{\varepsilon}} + J_{\theta\varepsilon}^T B_M \frac{\partial M^{aero}}{\partial\dot{\varepsilon}}, \quad \frac{\partial R_F^{aero}}{\partial\beta} = J_{p\varepsilon}^T B_F \frac{\partial F^{aero}}{\partial\beta} + J_{\theta\varepsilon}^T B_M \frac{\partial M^{aero}}{\partial\beta}$$

$$\frac{\partial R_F^{aero}}{\partial\varepsilon} = J_{p\varepsilon}^T B_F \frac{\partial F^{aero}}{\partial\varepsilon} + J_{\theta\varepsilon}^T B_M \frac{\partial M^{aero}}{\partial\varepsilon}, \qquad (38)$$

$$\frac{\partial R_B^{aero}}{\partial\ddot{\varepsilon}} = J_{pb}^T B_F \frac{\partial F^{aero}}{\partial\ddot{\varepsilon}} + J_{\theta b}^T B_M \frac{\partial M^{aero}}{\partial\ddot{\varepsilon}}, \quad \frac{\partial R_B^{aero}}{\partial\dot{\beta}} = J_{pb}^T B_F \frac{\partial F^{aero}}{\partial\dot{\beta}} + J_{\theta b}^T B_M \frac{\partial M^{aero}}{\partial\dot{\beta}}$$

$$\frac{\partial R_B^{aero}}{\partial\dot{\varepsilon}} = J_{pb}^T B_F \frac{\partial F^{aero}}{\partial\dot{\varepsilon}} + J_{\theta b}^T B_M \frac{\partial M^{aero}}{\partial\dot{\varepsilon}}, \quad \frac{\partial R_B^{aero}}{\partial\beta} = J_{pb}^T B_F \frac{\partial F^{aero}}{\partial\beta} + J_{\theta b}^T B_M \frac{\partial M^{aero}}{\partial\beta}$$

Therefore, Eq. (37) can be written as

$$\bar{M}_{FF}\ddot{\varepsilon} + \bar{M}_{FB}\dot{\beta} + \bar{C}_{FF}\dot{\varepsilon} + \bar{C}_{FB}\beta + \bar{K}_{FF}\varepsilon - R_{F/\lambda_0}^{aero}\lambda - R_{F/\zeta_0}^{grav}\zeta = 0$$

$$\bar{M}_{BF}\ddot{\varepsilon} + \bar{M}_{BB}\dot{\beta} + \bar{C}_{BF}\dot{\varepsilon} + \bar{C}_{BB}\beta - R_{B/\lambda_0}^{aero}\lambda - R_{B/\zeta_0}^{grav}\zeta = 0$$

$$\dot{\zeta} + \frac{1}{2}\Omega_\zeta\zeta + \frac{1}{2}\left(\Omega_{\zeta/\beta_0}\beta\right)\zeta_0 = 0 \qquad (39)$$

$$\dot{P}_B - \begin{bmatrix} C^{GB} & 0 \end{bmatrix}\beta - \left[\left(C_{/\zeta_0}^{GB}\zeta\right) \quad 0\right]\beta_0 = 0$$

$$\dot{\lambda} - F_1\begin{bmatrix}\ddot{\varepsilon}\\\dot{\beta}\end{bmatrix} - F_2\begin{bmatrix}\dot{\varepsilon}\\\beta\end{bmatrix} - F_3\lambda = 0$$

where

$$\bar{M}_{FF} = M_{FF} - J_{p\varepsilon}^T B_F \frac{\partial F^{aero}}{\partial \ddot{\varepsilon}} - J_{\theta\varepsilon}^T B_M \frac{\partial M^{aero}}{\partial \ddot{\varepsilon}}$$

$$\bar{M}_{FB} = M_{FB} - J_{p\varepsilon}^T B_F \frac{\partial F^{aero}}{\partial \dot{\beta}} + J_{\theta\varepsilon}^T B_M \frac{\partial M^{aero}}{\partial \dot{\beta}}$$

$$\bar{C}_{FF} = C_{FF} + \frac{\partial C_{FF}}{\partial \dot{\varepsilon}} \dot{\varepsilon}_0 + \frac{\partial C_{FB}}{\partial \dot{\varepsilon}} \beta_0 - J_{p\varepsilon}^T B_F \frac{\partial F^{aero}}{\partial \dot{\varepsilon}} - J_{\theta\varepsilon}^T B_M \frac{\partial M^{aero}}{\partial \dot{\varepsilon}}$$

$$\bar{C}_{FB} = C_{FB} + \frac{\partial C_{FF}}{\partial \beta} \dot{\varepsilon}_0 + \frac{\partial C_{FB}}{\partial \beta} \beta_0 - J_{p\varepsilon}^T B_F \frac{\partial F^{aero}}{\partial \beta} - J_{\theta\varepsilon}^T B_M \frac{\partial M^{aero}}{\partial \beta}$$

$$\bar{K}_{FF} = K_{FF} - J_{p\varepsilon}^T B_F \frac{\partial F^{aero}}{\partial \varepsilon} - J_{\theta\varepsilon}^T B_M \frac{\partial M^{aero}}{\partial \varepsilon}$$

(40)

and

$$\bar{M}_{BF} = M_{BF} - J_{pb}^T B_F \frac{\partial F^{aero}}{\partial \ddot{\varepsilon}} - J_{\theta b}^T B_M \frac{\partial M^{aero}}{\partial \ddot{\varepsilon}}$$

$$\bar{M}_{BB} = M_{BB} - J_{pb}^T B_F \frac{\partial F^{aero}}{\partial \dot{\beta}} - J_{\theta b}^T B_M \frac{\partial M^{aero}}{\partial \dot{\beta}}$$

$$\bar{C}_{BF} = C_{BF} + \frac{\partial C_{BF}}{\partial \dot{\varepsilon}} \dot{\varepsilon}_0 + \frac{\partial C_{BB}}{\partial \dot{\varepsilon}} \beta_0 - J_{pb}^T B_F \frac{\partial F^{aero}}{\partial \dot{\varepsilon}} - J_{\theta b}^T B_M \frac{\partial M^{aero}}{\partial \dot{\varepsilon}}$$

$$\bar{C}_{BB} = C_{BB} + \frac{\partial C_{BF}}{\partial \beta} \dot{\varepsilon}_0 + \frac{\partial C_{BB}}{\partial \beta} \beta_0 - J_{pb}^T B_F \frac{\partial F^{aero}}{\partial \beta} - J_{\theta b}^T B_M \frac{\partial M^{aero}}{\partial \beta}$$

(41)

Finally, Eq. (39) can be put into state space form

$$\begin{bmatrix} \dot{\varepsilon} & \ddot{\varepsilon} & \dot{\beta} & \dot{\zeta} & \dot{P}_B & \dot{\lambda} \end{bmatrix}^T = Q_1^{-1} Q_2 \begin{bmatrix} \varepsilon & \dot{\varepsilon} & \beta & \zeta & P_B & \lambda \end{bmatrix}^T = A \begin{bmatrix} \varepsilon & \dot{\varepsilon} & \beta & \zeta & P_B & \lambda \end{bmatrix}^T \qquad (42)$$

or

$$\dot{x} = Ax \qquad (43)$$

where

$$x = \begin{bmatrix} \varepsilon & \dot{\varepsilon} & \beta & \zeta & P_B & \lambda \end{bmatrix}^T \qquad (44)$$

and

$$Q_1 = \begin{bmatrix} I & 0 & 0 & 0 & 0 & 0 \\ 0 & \bar{M}_{FF} & \bar{M}_{FB} & 0 & 0 & 0 \\ 0 & \bar{M}_{BF} & \bar{M}_{BB} & 0 & 0 & 0 \\ 0 & 0 & 0 & I & 0 & 0 \\ 0 & 0 & 0 & 0 & I & 0 \\ 0 & -F_{1F} & -F_{1B} & 0 & 0 & I \end{bmatrix}, \qquad Q_2 = \begin{bmatrix} 0 & I & 0 & 0 & 0 & 0 \\ -\bar{K}_{FF} & -\bar{C}_{FF} & -\bar{C}_{FB} & R_{F/\zeta_0}^{grav} & 0 & R_{F/\lambda_0}^{aero} \\ 0 & -\bar{C}_{BF} & -\bar{C}_{BB} & R_{B/\zeta_0}^{grav} & 0 & R_{B/\lambda_0}^{aero} \\ 0 & 0 & -\frac{1}{2}\Omega_{\zeta/\beta_0}\zeta_0 & -\frac{1}{2}\Omega_\zeta & 0 & 0 \\ 0 & 0 & \begin{bmatrix} C^{GB} & 0 \end{bmatrix} & \begin{bmatrix} C_{/\zeta_0}^{GB} & 0 \end{bmatrix}\beta_0 & 0 & 0 \\ 0 & F_{2F} & F_{2B} & 0 & 0 & F_3 \end{bmatrix} \qquad (45)$$

G. Solution for the Stability Boundary

The nonlinear stability analysis is conducted in an iterative way, as indicated in Fig. 5. Starting from a predefined flight condition, the system is brought to the nonlinear steady state and linearized about the condition. Eigenvalue analysis of the resulting system matrix A in Eq. (42) is performed. Eigenvalues with positive real parts indicate instability. The speed is increased and the process is repeated until the instability is reached. One may use the same system matrix for different solution types of stability analysis, such as flutter of free flight vehicles, flutter of vehicles with constrained rigid body motions, or the flight dynamic stability. To do so, one needs to choose the appropriate subset of the system matrix.
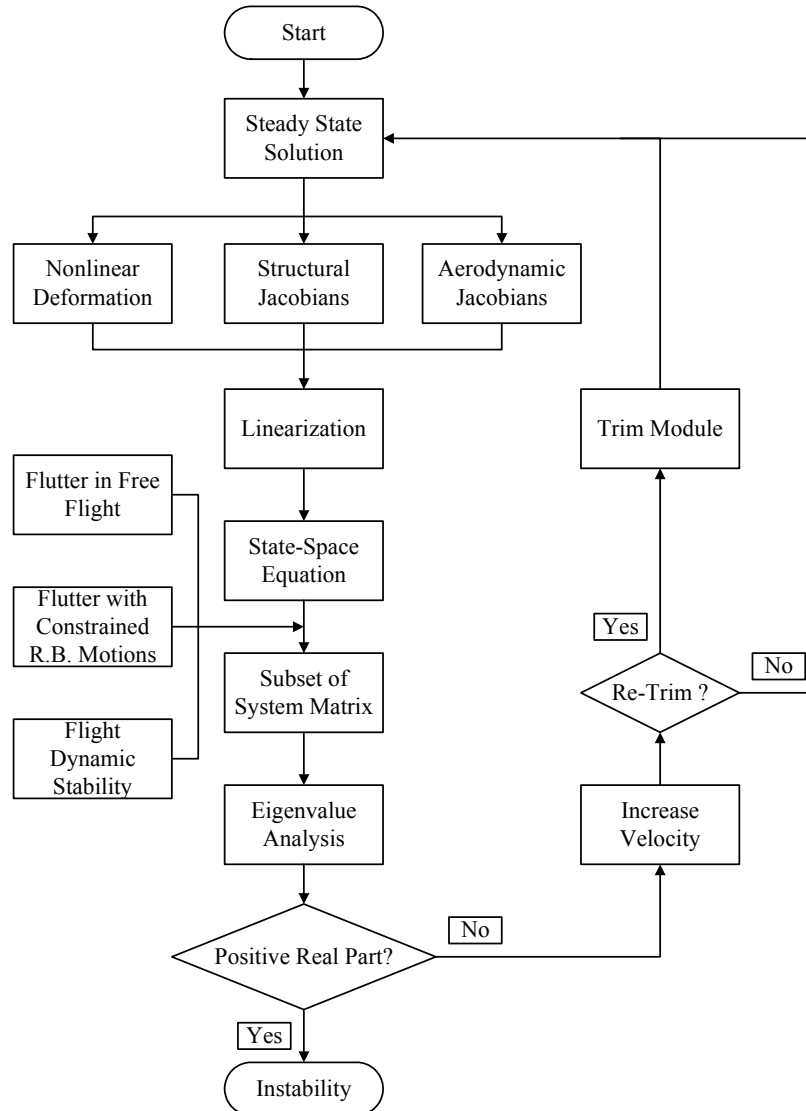
Figure 5. Scheme of searching for the stability boundary

III.   Numerical Studies

A baseline blended-wing-body model is developed for this study. The wing and body properties are modified from the half wing wind-tunnel model described in Ref. 16, while the model is completed as a symmetric vehicle. This configuration serves the testbed for the numerical studies presented here, focusing on its stability and gust response.

A. Geometry

Figure 6 shows the geometry of the blended-wing-body model. Both body and wing are modeled as beams coupled with aerodynamics. The red dashed-dotted line indicates the location of the beam reference axis. The shear center of the beam varies from the body's root (64.38% of the chord) to the wing root (45.60% of the chord), and keeps its relative position unchanged along the wing. Physical parameters of the body and wings are listed in Table 1. One balance weight of 80 kg is positioned at the center of the model, 0.89 m ahead of the reference line. In addition, nine nonstructural masses, each 2 kg, are evenly distributed along the wing from the root to the tip. The wing contains three independent elevons, as indicated in Fig. 6. These elevons occupy 25% of the chord from wing root to 75% span of the wing.
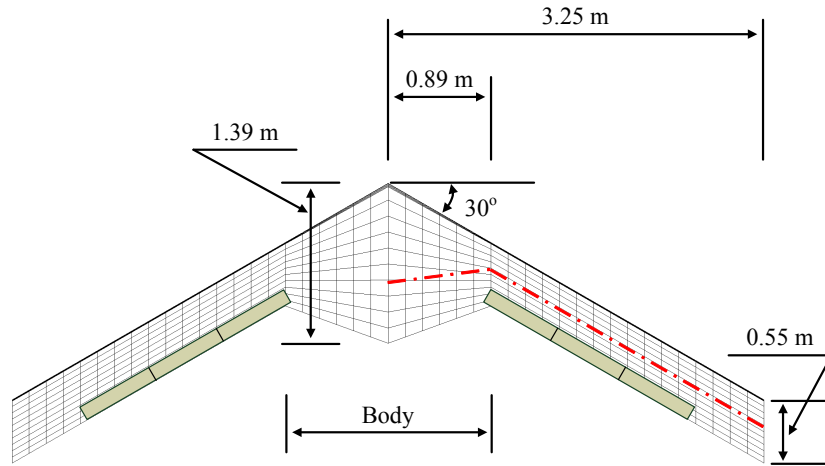
Figure 6. Geometry of the blended-wing-body model

Table 1.   Properties of the body and wing members of the blended-wing-body model

	Body	Wing
Ref. axis location (root/tip) (From L.E.)	64.38% / 45.60% chord	45.60% / 45.60% chord
Center of gravity (root/tip) (From L.E.)	64.38% / 45.60% chord	45.60% / 45.60% chord
Extension rigidity	1.69×10^8 N	1.55×10^8 N
Flat bending rigidity	7.50×10^5 N·m^2	1.14×10^4 N·m^2
Chord bending rigidity	3.50×10^7 N·m^2	1.30×10^5 N·m^2
Torsional rigidity	2.25×10^6 N·m^2	1.10×10^4 N·m^2
Mass per unit length	50.00 kg/m	6.20 kg/m
Flat bending inertia per unit length	0.70 kg·m	5.00×10^{-4} kg·m
Edge bending inertia per unit length	22.00 kg·m	4.63×10^{-3} kg·m
Rotational inertia per unit length	4.50 kg·m	5.08×10^{-3} kg·m

B. System Modes and Frequencies

To assess the vehicle's flight characteristic, the full aeroelastic/flight dynamic equations of motion are linearized at different trimmed flight conditions. Longitudinal flight modes are then evaluated using each linearized equation. Figure 7 shows the longitudinal modes of the vehicle at different altitudes and flight speed. It can be seen that both the phugoid and short-period modes are stable at the evaluated range (0 – 15,000 m, 0.2 – 0.7 M). The root locus of the phugoid mode has the tendency to cross the imaginary axis with the increase of Mach number, while its frequency is reduced. On the other side, the root locus of the short-period mode extends away from the imaginary axis when the speed is increased, and the corresponding frequency grows up. At a given speed (say 0.4 M, circles in the figure), the damping of the phugoid mode negatively increases with altitude, which indicates larger stability margin. However, this trend for the short-period mode is reversed.

Table 2 lists the first few fundamental modes of the elastic wing and body. It is easy to find that the frequency of the first flatwise bending mode is right within the variation range of the short-period mode, which means a coupling of these two modes is possible.
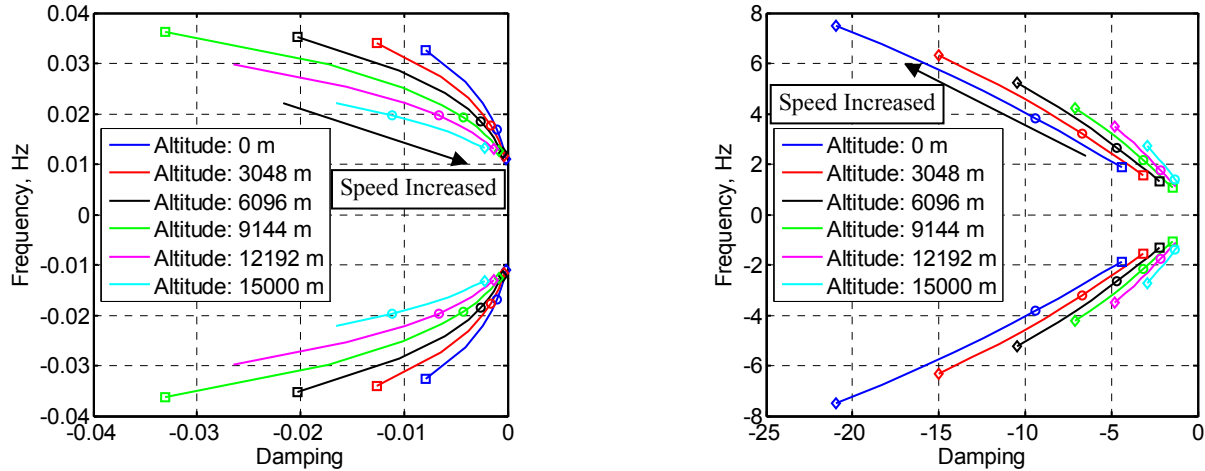
Figure 7. Root locus of phugoid mode (left) and short-period mode (right) of the blended-wing-body configuration at different altitude, speed from 0.2 M (square) to 0.7 M (diamond)

Table 2.   Fundamental modes and frequencies of the elastic wing and body

No.	Mode	Frequency (Hz)
1	1st flatwise bending	3.3
2	1st edgewise bending	10.9
3	2nd flatwise bending	20.4
4	3rd flatwise bending	55.6
5	2nd edgewise bending	69.5
6	4th flatwise bending	82.0

C. Flutter Boundary of Cantilevered Half-Span Model

In this analysis, aeroelastic instabilities of the blended-wing-body aircraft are to be identified over a range of flight conditions, using the proposed process described in Fig. 5. The body angle of a half-span model is varied from 0 to 8 degrees, without elevon deflections. However, the rigid-body degrees of freedom are all constrained. This setup simulates the basic test setup in the wind-tunnel. The simulation also considers different altitudes (from sea level to 15,000 m altitude). Results obtained are summarized in Figs. 8 to 10.
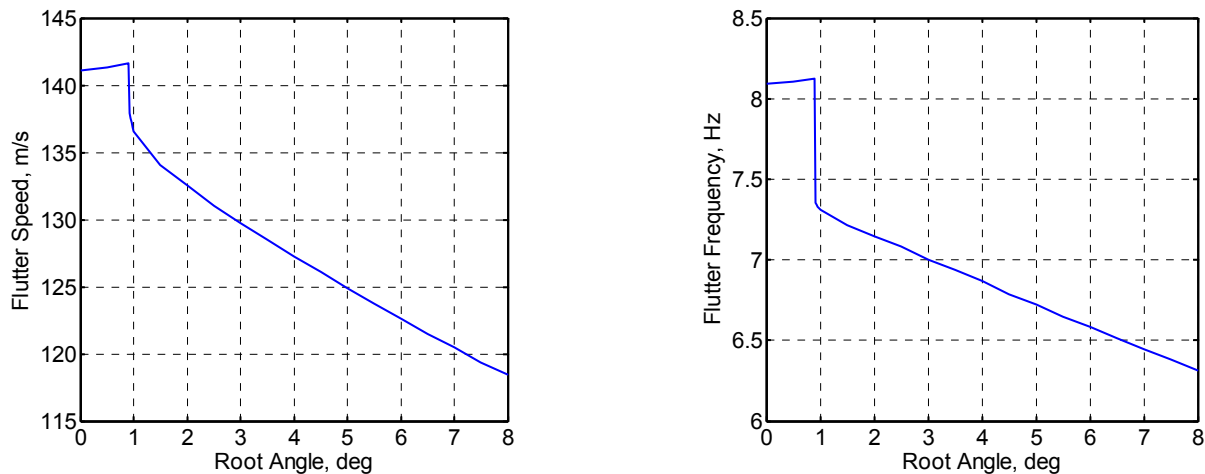
Figure 8. Flutter speed and frequency at sea level

By observing the plots of flutter boundaries, one may find different trends at different altitudes. At sea level, the flutter speed is initially slightly increased when the root angle is increased. When a critical value of the angle is reached, the flutter boundary is significantly reduced with the increase of the root angle. When the root angle is low, the flutter mode is a coupled flatwise bending and torsion of the wing. There is nearly no in-plane bending component in the flutter mode (see Fig. 11). However, when the root angle is larger than the critical value, the in-plane bending participates in the unstable mode, as shown in Fig. 12. This change of flutter mode does not happen when the altitude is high (6,096 and 15,000 m altitude), where the flutter modes are always coupled flatwise bending, in-plane bending and torsion, which are similar to the one shown in Fig. 12.
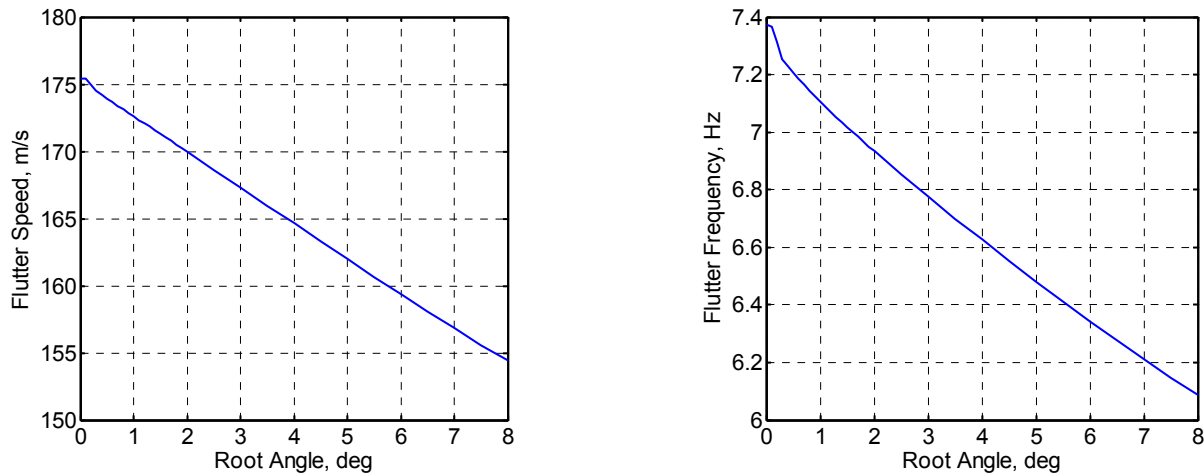
Figure 9. Flutter speed and frequency at 6,096 m altitude
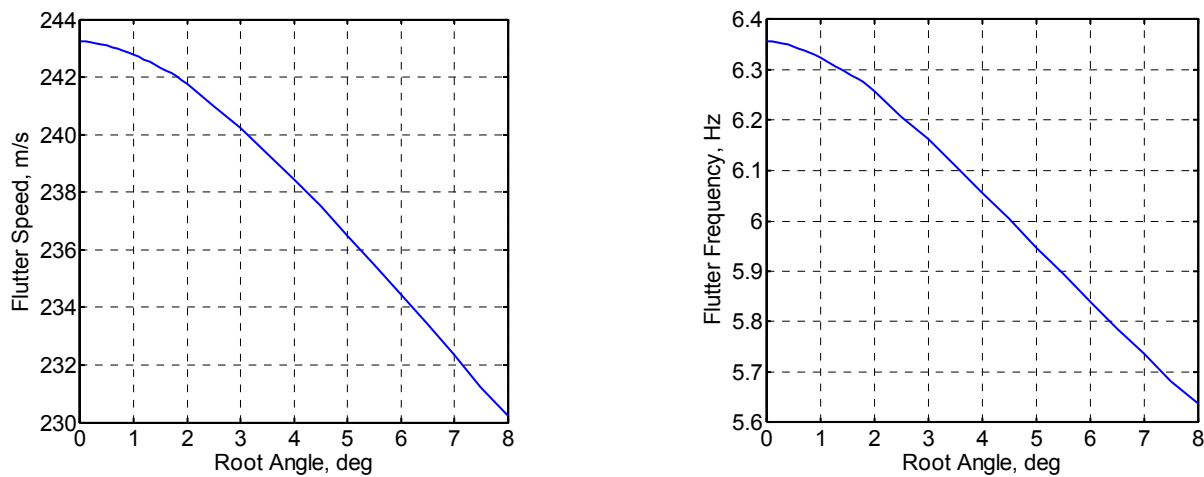
Figure 10. Flutter speed and frequency at 15,000 m altitude
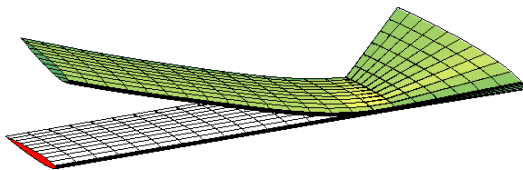
Figure 11. Flutter mode shape change at sea level with zero root angle
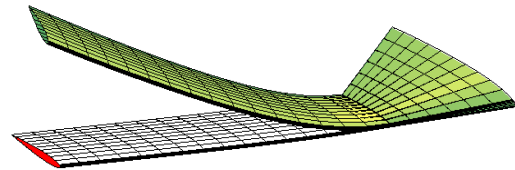
Figure 12. Flutter mode shape change at sea level with 2° root angle

To verify the nonlinear flutter boundary calculation presented above, two individual time domain simulation are performed. With the altitude of 6,096 m, and the root angle of 8°, one of the simulations has a flow velocity (147 m/s) under the flutter speed (154.39 m/s), while the other simulates with a slightly higher flow velocity (162 m/s) than the flutter speed. The time histories of the tip displacements are plotted in Figs. 13 and 14, respectively. From Fig. 13, the wing deformation of the pre-flutter case is stabilized after some initial oscillations. However, the wing oscillation is self-excited for the post-flutter case, as seen from Fig. 14. The amplitude of the wing oscillation is increased, until it goes into a limit cycle oscillation.
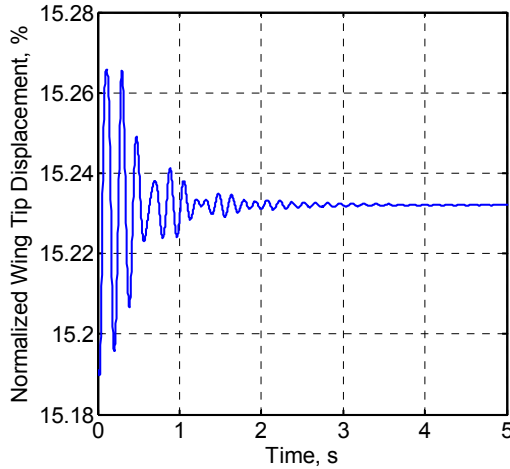
Figure 13.   Wing tip displacement, speed 147 m/s, altitude 6,096 m, root angle 8°
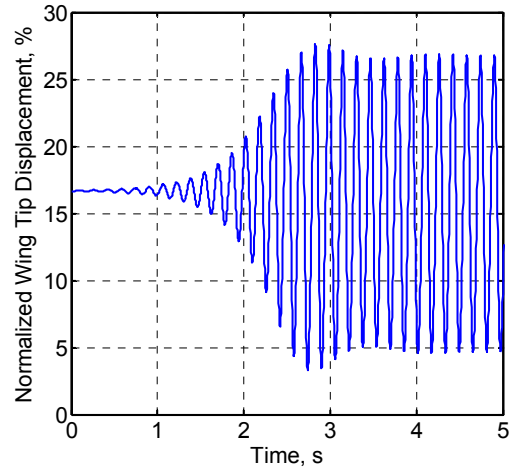
Figure 14.   Wing tip displacement, speed 162 m/s, altitude 6,096 m, root angle 8°

D. Flutter Boundary of Full Vehicle in Flight

As have been discussed before, the wings of this vehicle are flexible in such a way that their elastic modes are coupled with the rigid-body modes of the whole vehicle. Therefore, the evaluation of the stability of the full vehicle should include the rigid-body degrees of freedom, which gives the stability boundary in flight.

As an example, the full vehicle's stability is evaluated at 6,096 m altitude for the level flight condition, *i.e.*, the vehicle is trimmed for every flight speeds where the stability is checked. In order to assess the coupling between the wing elastic deformation and the rigid-body motions, multiple constraints to the rigid-body motions are used when calculating the flutter boundary. First, the vehicle has all rigid-body motions constrained (Case 1), and then plunging motion is set free (Case 2), followed by another case with both plunging and pitching set free (Case 3). Finally, all rigid-body motions are free and coupled with the wing deformations (Case 4).

The flutter speeds and frequencies of the corresponding flutter mode for the four different cases are listed in Table 3. These results were obtained using the proposed process described in Fig. 5. The root locus of Case 1 and 4 are plotted in Figs. 15 and 16. Since the unstable mode for the free flight vehicle (Case 4) is the wing bending/torsion coupled with both pitching and plunging motions (see Fig. 17), its flutter speed is nearly identical to the case with only pitching and plunging set free (Case 3). For the case when only plunging is free, there is no coupling between wing deformation and the pitching of the body, which result in a weak coupling between the wing elastic deformation and the free rigid-body motion. That flutter boundary is the closest to the case with the rigid-body motions fully constrained.

Table 3.   Flutter boundaries for different rigid-body motion constraints

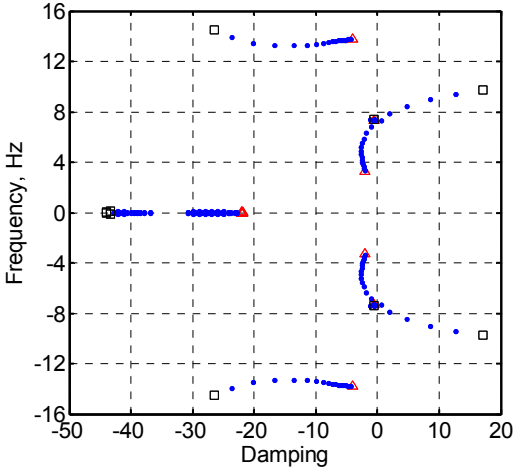|	Constraint	Flutter speed (m/s)	Frequency (Hz)
Case 1	Fully constrained	172.52	7.30
Case 2	Free plunging only	164.17	7.07
Case 3	Free pitching/plunging	123.17	3.32
Case 4	Free flight	123.20	3.32

Figure 15. Root locus of the fully-constrained case, speed from 100 m/s (triangle) to 200 m/s (square)
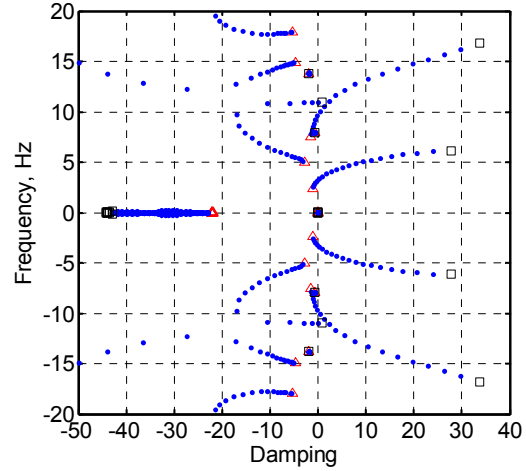

Figure 16. Root locus of the free-flight case, speed from 100 m/s (triangle) to 200 m/s (square)
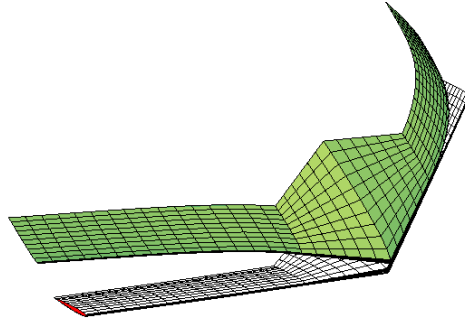

Figure 17. Flutter mode shape of the free-flight case

In time domain, two individual simulations are carried out for verification purposes, one of which simulates the level flight of the vehicle with a flight velocity lower than the flutter speed (120 m/s), while the other flies with a slightly higher velocity (125 m/s) than the flutter speed. A sinusoidal deflection of all the three elevons is used as perturbation, which is governed by

$$\delta = \begin{cases} 0 & t < 0.5 \\ -0.1\sin 2\pi t & \text{(deg)} \quad 0.5 \leq t \leq 1.5 \\ 0 & t > 1.5 \end{cases} \tag{46}$$

The time histories of the tip displacements and body frame pitching angles are plotted in Figs. 18 to 21. For the pre-flutter case (Figs. 18 and 19), the responses converged after initial oscillations. However, the responses of the post-flutter case diverged, showing instability, as shown in Figs. 20 and 21. As one can see from Fig. 21, the pitching motion is not stable, which is correctly predicted by the frequency domain flutter calculation. One more observation from the time domain simulation is that the frequency of the unstable oscillation is approximately 3.33 Hz, which agrees with the frequency-domain prediction very well.

American Institute of Aeronautics and Astronautics
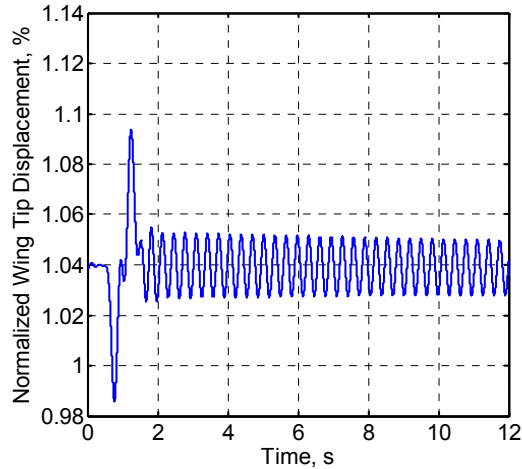
Figure 18. Normalized wing tip displacement of the pre-flutter case for the blended-wing-body vehicle, speed 120 m/s
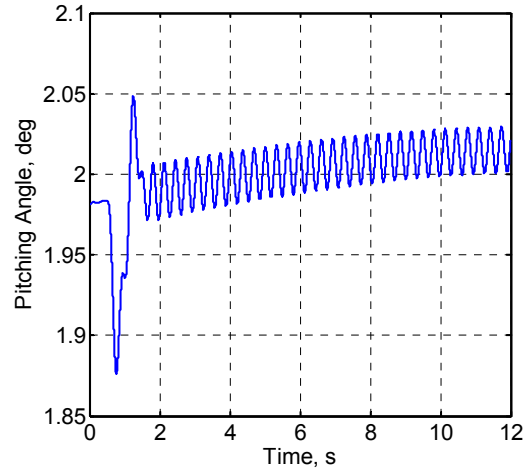
Figure 19. Body frame pitching angle of the pre-flutter case for the blended-wing-body vehicle, speed 120 m/s
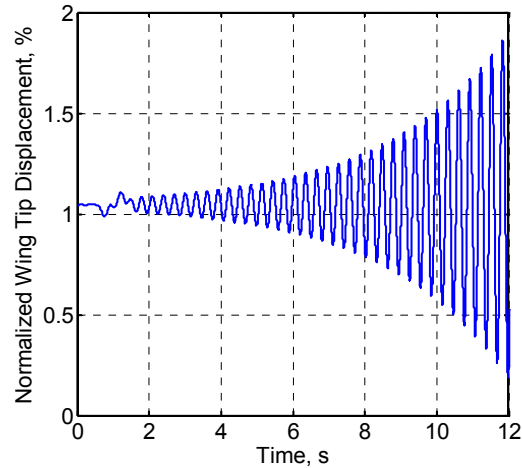
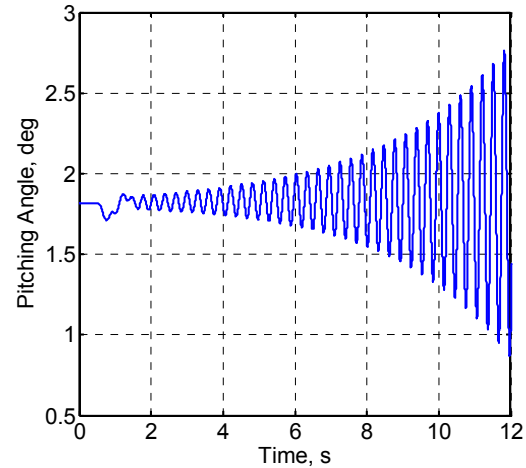**Figure 20.** Normalized Wing tip displacement of the post-flutter case for the blended-wing-body vehicle, speed 125 m/s

Figure 21. Body frame pitching angle of the post-flutter case for the blended-wing-body vehicle, speed 125 m/s

E. Response of the Vehicle to Gust Perturbations

To better understand the aeroelastic and flight dynamic characteristics, the vehicle is simulated under gust perturbations. The simulation is conducted at 6,096 m with the flight speed of 110.64 m/s (0.35 M). A discrete gust model is used, whose spatial distribution is governed by a 1-cosine function, with the maximum gust speed of 15.24 m/s (50 ft/s), and the gust region along the flight path extending for 13.72 m, which is approximately 25 times wing chord lengths. The gust is symmetrically applied to the vehicle. Note that stall effects are considered through a simplified stall model[6], when the local angle of attack at an airfoil reaches the critical stall angle.

There are three types of simulation considered:
1) Nonlinear simulation with follower aerodynamic loads (Sim 1);
2) Linearized simulation with follower aerodynamic loads (Sim 2);
3) Linearized simulation with fixed-direction aerodynamic loads (Sim 3).

The simulation results are compared in Figs. 22 to 27. It can be seen that the applied gust perturbation does not excite any instability of the vehicle. The phugoid mode can be clearly observed from the plots of longitudinal velocity (Fig. 22) and altitude (Fig. 26). This mode is stable and slightly damped. One may measure the period of the phugoid mode and only the period from nonlinear simulation with follower aerodynamic loads (Sim 1) agrees

American Institute of Aeronautics and Astronautics

with what has been predicted from the frequency-domain analysis (see Fig. 7). The other two simulations give the results that are slightly off, with significant difference in oscillation amplitudes. For the linearized simulation with fixed-direction aerodynamic loads (the black dotted line in Fig. 26), the vehicle altitude is not recovered after one cycle. Therefore, it does not simulate the motion associated with the phugoid mode accurately.

The high-frequency response at the initial times is associated with the short-period mode excited by the gust perturbation. The amplitude of this oscillation decays quickly with a high negative damping. One may find the short-period mode frequency (Fig. 24) is quite close to that of the wing elastic oscillation (Fig. 27), which indicates coupling between the two motions.

To step further into the analysis, the gust amplitude is increased to be double the nominal one. The results of the nonlinear simulation with follower aerodynamic loads are compared with the one with nominal gust, which are plotted in Fig. 28. It can be noticed that the gust amplitude does not change the characteristics of the response. The frequency of the stable phugoid mode is nearly the same as the simulation with nominal gust.

In order to study the effects of the gust on the vehicle response at sub-critical conditions, the flight speed of the vehicle is increased to 122 m/s, which is approximately 1% lower than the flutter boundary. The same nominal gust is used for the nonlinear simulation with follower aerodynamic loading. The results are compared with another simulation, in which the vehicle flies in calm air (see Figs. 29 to 34). One may find the flight in calm air is stable, as the speed is lower than the flutter boundary. However, the finite gust perturbation brings instability to the whole system. The vehicle sinks due to the gust perturbation and the flight velocity is increased to be greater than the flutter boundary after 15 seconds, where the short-period mode coupled with the wing elastic bending deformation grows to be unstable. Eventually, this motion develops into a beating oscillation (see Figs. 31, 32, and 34).
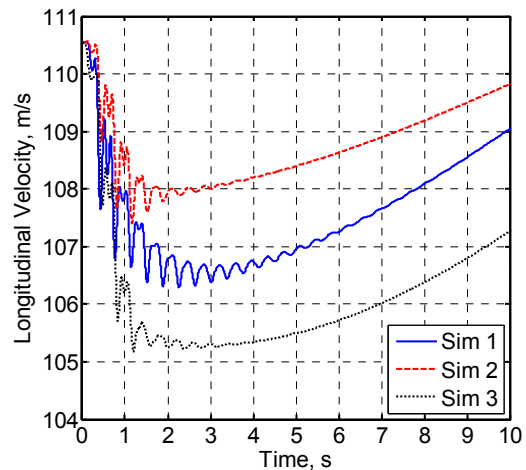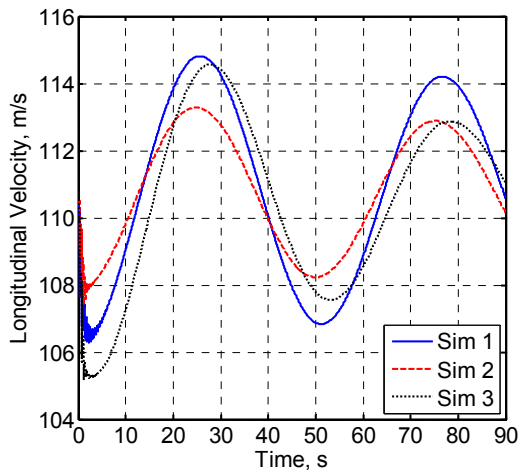

Figure 22. **Body frame longitudinal velocity with gust perturbation for different simulation cases (zoomed for initial times on the right)**
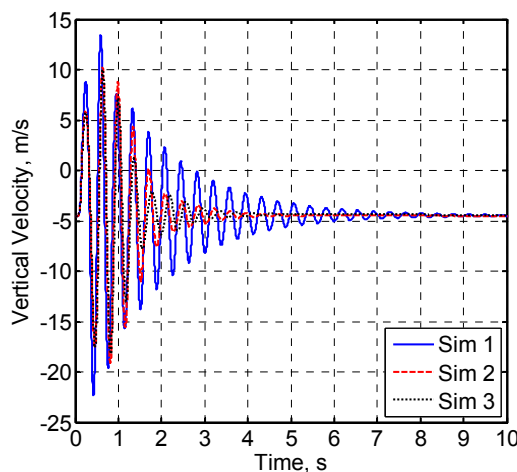

Figure 23. **Body frame vertical velocity with gust perturbation for different simulation cases**
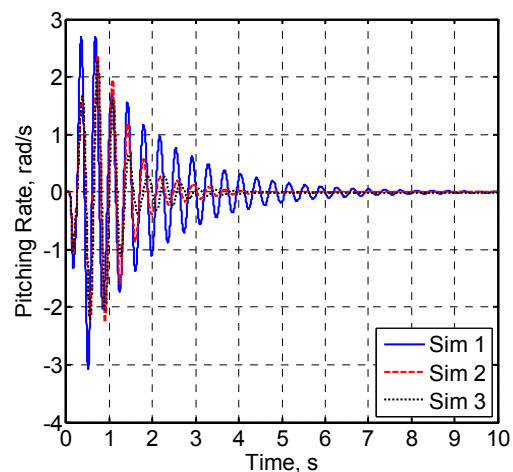
Figure 24. **Body frame pitching rate with gust perturbation for different simulation cases**

20

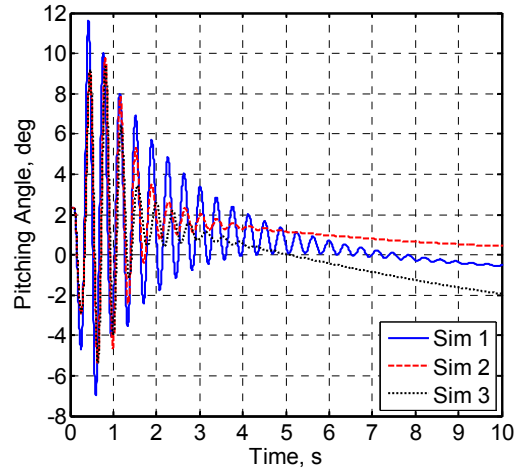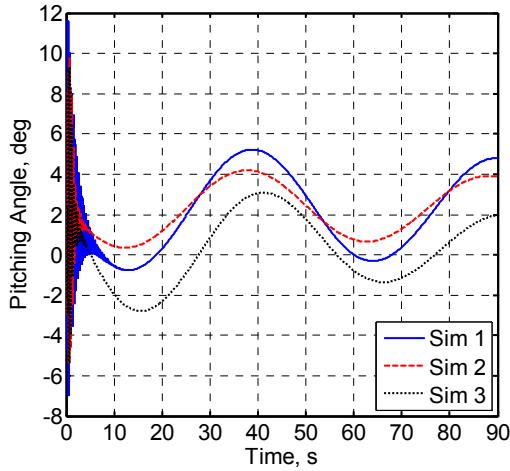American Institute of Aeronautics and Astronautics

Figure 25. **Body frame pitching angle with gust perturbation for different simulation cases (zoomed for initial times on the right)**
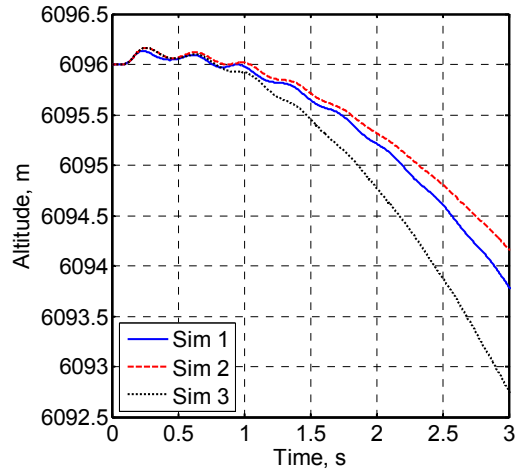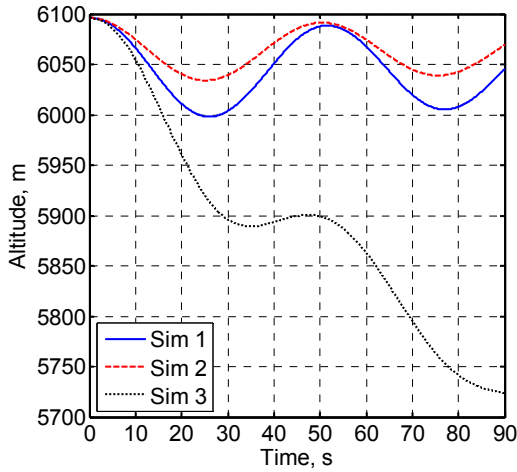

Figure 26. **Altitude change with gust perturbation for different simulation cases (zoomed for initial times on the right)**
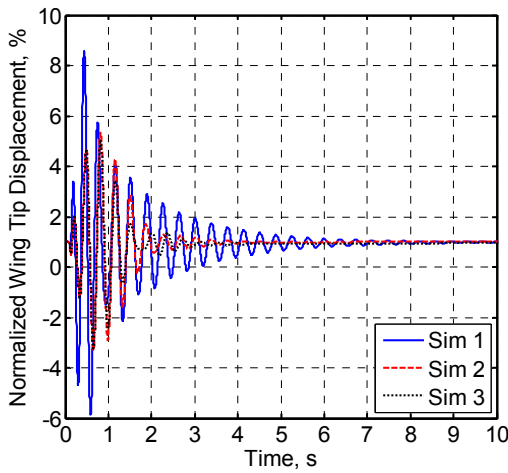

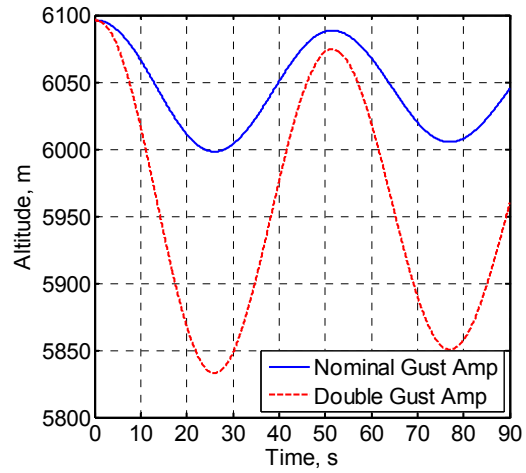**Figure 27.** **Normalized wing tip displacement with gust perturbation for different simulation cases**

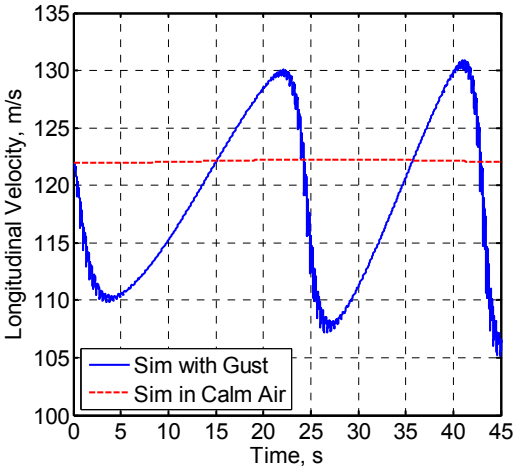**Figure 28.** **Altitude change with different gust amplitudes**

Figure 29. Body frame longitudinal velocity with gust perturbation at sub-critical condition
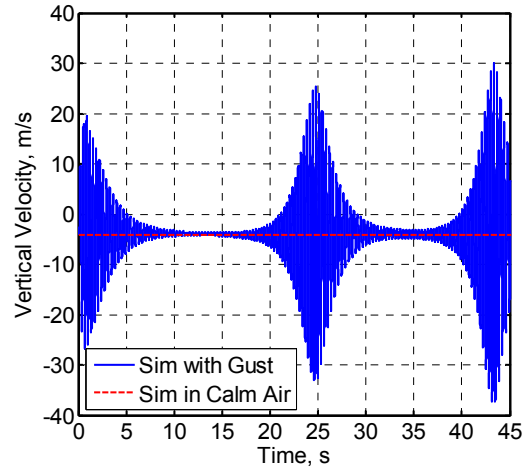

Figure 30. Body frame vertical velocity with gust perturbation at sub-critical condition
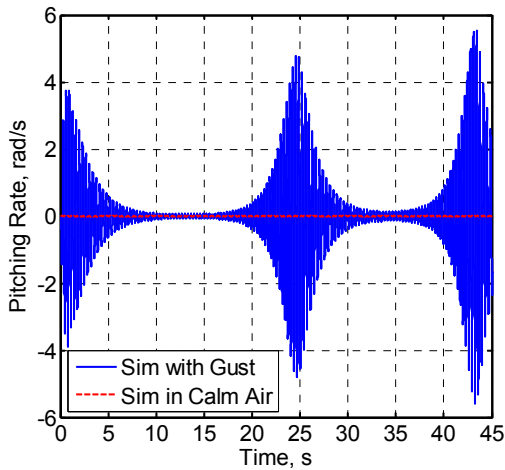

Figure 31. Body frame pitching rate with gust perturbation at sub-critical condition
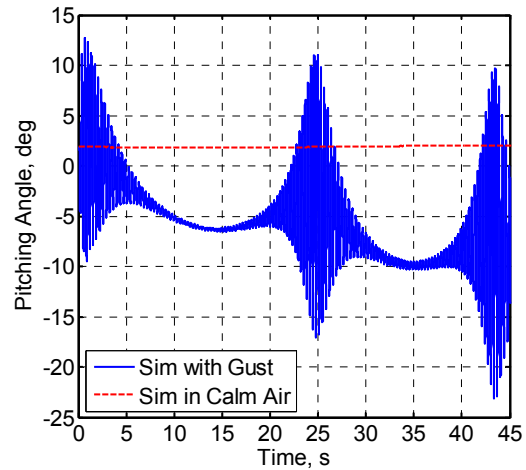

Figure 32. Body frame pitching angle with gust perturbation at sub-critical condition
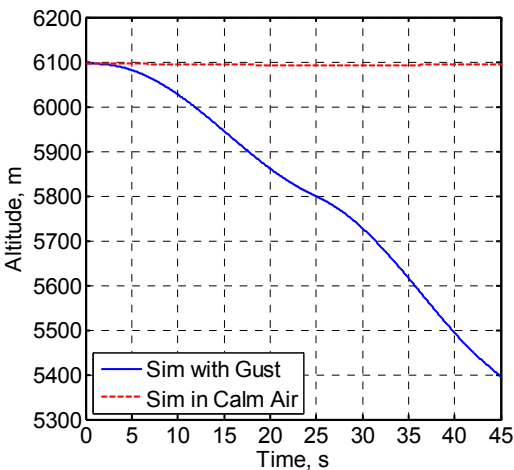

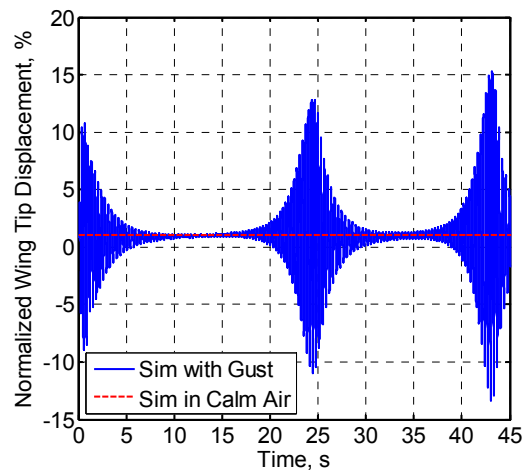**Figure 33. Altitude change with gust perturbation at sub-critical condition**

Figure 34. Normalized wing tip displacement with gust perturbation at sub-critical condition

F. Aeroelastic Tailoring

In the nominal blended-wing-body model, there is no coupling between torsional and out-of-plane bending stiffness of the wing. A tuning parameter (α) is used for the tailoring of the wing stiffness, such that the torsional/out-of-plane bending stiffness K_{23} is determined by the following relation

$$K_{23} = \alpha\sqrt{K_{22} \cdot K_{33}} \qquad \alpha = 0, \ \pm 0.25, \ \pm 0.50, \ \pm 0.75 \tag{47}$$

The change of torsional/out-of-plane coupling may impact the vehicle's stability boundary. In order to evaluate the impact, the flutter boundary of the vehicle in free flight condition (level flight at 6,096 m altitude, no constraints in rigid-body degrees of freedom) is calculated for configurations with different coupling levels. The variation of the flutter boundary is plotted in Fig. 35. By looking at the unstable mode shapes for these configurations, one may find the shift of flutter mode when the tuning parameter is changed from positive to negative. If the coupling between torsion and out-of-plane bending stiffness is positive, the flutter modes are the same as the nominal configuration, as shown in Fig. 17. However, if the coupling is negative, the flutter modes are switched to the roll motion of the body with complex in-plane/out-of-bending and twist of the wing, as described in Fig. 36. It is also noticeable that the flutter boundary is more sensitive to the positive coupling coefficient (wash in) than the negative one (wash out). When the tuning parameter is positive 0.75, the flutter speed is reduced to less than half of the nominal configuration. Also, no higher flutter speed was found than the one with α equals zero.
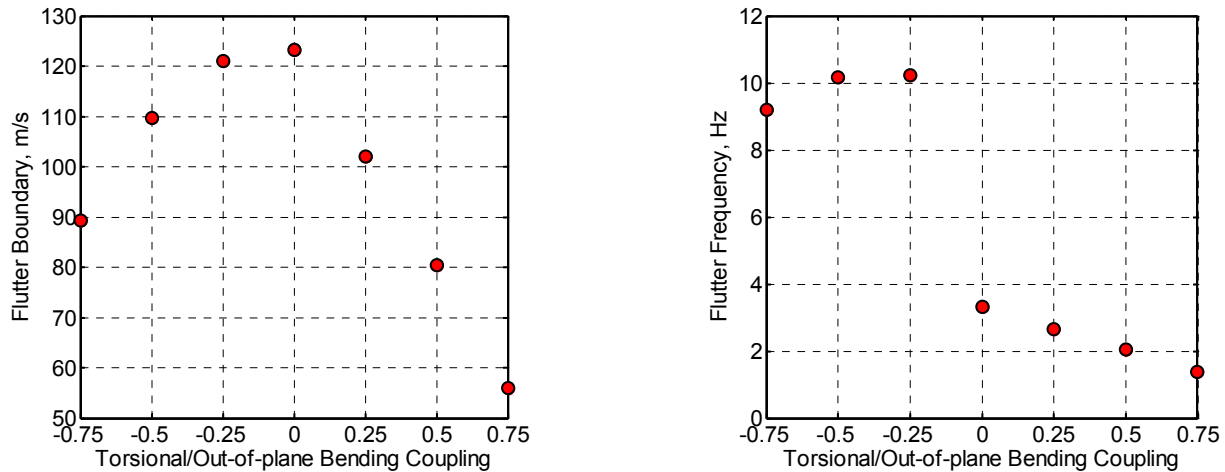

Figure 35.   Change of flutter speed and frequency in free flight with different twist/out-of-plane bending coupling
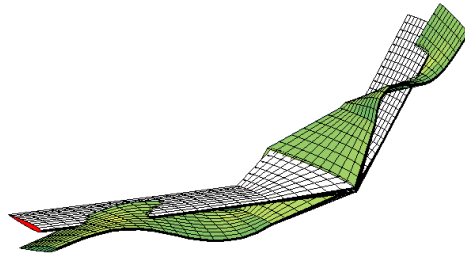

Figure 36.   Anti-symmetric mode shape with -0.75 tuning parameter

IV. Concluding Remarks

In this paper, the coupled nonlinear flight dynamic and aeroelastic characteristics of a blended-wing-body aircraft are described by a set of nonlinear equations. The geometrically-nonlinear structural model is a strain-based

formulation, which is able to capture the large deformations of slender structures. Finite-state unsteady subsonic aerodynamic loads with compressibility correction are coupled with the structural formulation, which completes the aeroelastic formulation. Nonlinear equations of motion for a frame associated to the vehicle (not necessarily at its *c.g.* point) complete the coupled flight dynamics/aeroelastic formulation. With these equations, fully nonlinear time-marching analysis can be performed to study the time-domain characteristics. The nonlinear equations can also be linearized about a given nonlinear state. The resulting linear equations can be put into state-space form, such that stability boundary and flight dynamic modes can be assessed.

Longitudinal flight dynamic modes are studies for a sample model vehicle with the Mach number ranging from 0.2 to 0.7 at different altitudes. In the studied range, the phugoid and short-period modes of this vehicle are both stable. However, the elastic bending mode of the wing-body is low enough, such that it could be coupled with the short-period mode. That means the rigid-body motion could excite the instability of the wing-body system, which introduces a special type of dynamic instability – body-freedom flutter.

Enlightened by the above analyses, the flutter boundary of the whole vehicle is studies with different rigid-body constraints. For the particular vehicle studied here, the body-freedom flutter is excited due to the coupled short-period mode and wing elastic bending. As the wing oscillations are coupled with the rigid-body motion of the entire vehicle, the flutter boundary in free-flight condition differs from that of a constrained vehicle. Both the flutter boundary and the unstable modes obtained in free flight are different from the one in wind-tunnel tests when the rigid-body motions are fully constrained. This indicates that for the vehicles with flexible wing members, the flutter analysis should consider the whole vehicle's degrees of freedom, including the rigid-body modes. The traditional method by performing wind-tunnel tests to evaluate the flutter boundary may not be accurate.

To study the gust response, a spatial-distributed discrete gust model was seamlessly incorporated into the time simulation scheme. The gust perturbation is symmetrically applied to the vehicle. Three types of simulations were performed: 1) Nonlinear simulation coupled with follower aerodynamic loads; 2) Linearized simulation coupled with follower aerodynamic loads, and 3) Linearized simulation coupled with vertical aerodynamic loads. Only the nonlinear simulation with nonlinear aerodynamics can simulate the phugoid mode predicted in the frequency-domain analysis accurately. Moreover, the phugoid mode is not observed from the simulation with linear aerodynamics. This indicates the importance of the nonlinear analysis to the flight dynamic responses, especially the nonlinearity of the aerodynamics, even though the overall elastic deformation of the wings is small. The finite gust perturbation can bring instability to the vehicle that flies at sub-critical conditions.

There was no torsional/out-of-plane bending stiffness coupling in the nominal configuration. That was modified by tailoring the wings with different levels of bending/torsion coupling. For the example configuration, both the positive and negative couplings reduced the flutter boundary. However, the negative coupling introduced a different anti-symmetric flutter mode.

Acknowledgments

References

[1]Van Shoor, M. C., Zerweckh, S. H. and von Flotow, A. H., "Aeroelastic Stability and Control of a Highly Flexible Aircraft," AIAA-89-1187-CP, *Proceedings of 30th AIAA / ASME / ASCE / AHS / ASC Structures, Structural Dynamics and Materials Conference*, Mobile, AL, Apr. 3-5, 1989.

[2]Patil, M. J., Hodges, D. H. and Cesnik, C. E. S., "Nonlinear Aeroelasticity and Flight Dynamics of High-Altitude Long Endurance Aircraft," *Journal of Aircraft*, Vol. 38, No. 1, 2001, pp. 88-94.

[3]Drela, M., "Integrated Simulation Model for Preliminary Aerodynamic, Structural, and Control-Law Design of Aircraft," AIAA-99-1394, *Proceedings of 40th AIAA / ASME / ASCE / AHS / ASC Structures, Structural Dynamics, and Materials Conference and Exhibit*, St. Louis, MO, Apr. 12-15, 1999.

[4]Shearer, C. M. and Cesnik, C. E. S., "Nonlinear Flight Dynamics of Very Flexible Aircraft," *AIAA Atmospheric Flight Mechanics Conference and Exhibit*, San Francisco, CA, Aug. 15-18, 2005.

[5]Shearer, C. M. and Cesnik, C. E. S., "Modified Generalized Alpha Method for Integrating Governing Equations of Very Flexible Aircraft," *47th AIAA / ASME / ASCE / AHS / ASC Structures, Structural Dynamics, and Materials Conference*, Newport, RI, May 1-4, 2006.

[6]Su, W. and Cesnik, C. E. S., "Dynamic Response of Highly Flexible Flying Wings," *47th AIAA / ASME / ASCE / AHS / ASC Structures, Structural Dynamics, and Materials Conference*, Newport, RI, May 1-4, 2006.

[7]Tilmann, C. P., Flick, P. M., Martin, C. A. and Love, M. H., "High-Altitude Long Endurance Technologies for SensorCraft," *RTO AVT Symposium on Novel and Emerging Vehicle and Vehicle Technology Concepts*, Brussels, Belgium, Apr., 2003.

[8]Liebeck, R. H., Page, M. A. and Rawdon, B. K., "Blended-Wing-Body Subsonic Commercial Transport," *36th Aerospace Sciences Meeting & Exhibit*, Reno, NV, Jan. 12-15, 1998.

[9]Liebeck, R. H., "Blended Wing Body Design Challenges," *AIAA/ICAS International Air and Space Symposium and Exposition: The Next 100 Years*, Dayton, OH, Jul. 14-17, 2003.

[10]Mukhopadhyay, V., "Nonlinear Blended-Wing-Body (BWB) Fuselage Structural Design for Weight Reduction," *46th AIAA / ASME / ASCE / AHS / ASC Structures, Structural Dynamics, and Materials Conference*, Austin, TX, Apr. 18-21, 2005.

[11]Wakayama, S., "Multidisciplinary Design Optimization of the Blended-Wing-Body," *7th AIAA / USAF / NASA / ISSMO Symposium on Multidisciplinary Analysis and Optimization*, St. Louis, MO, Sep. 2-4, 1998.

[12]Wakayama, S., "Blended-Wing-Body Optimization Problem Setup," *8th AIAA / USAF / NASA / ISSMO Symposium on Multidisciplinary Analysis and Optimization*, Long Beach, CA, Sep. 6-8, 2000.

[13]Wakayama, S. and Kroo, I., "The Challenge and Promise of Blended-Wing-Body Optimization," *7th AIAA / USAF / NASA / ISSMO Symposium on Multidisciplinary Analysis and Optimization*, St. Louis, MO, Sep. 2-4, 1998.

[14]Ko, A., Leifsson, L. T., Mason, W. H., Schetz, J. A., Grossman, B. and Haftka, R. T., "MDO of a Blended-Wing-Body Transport Aircraft with Distributed Propulsion," *AIAA's 3rd Annual Aviation Technology, Integration, and Operations (ATIO) Tech*, Denver, CO, Nov. 17-19, 2003.

[15]Beran, P. S., Hur, J. Y., Snyder, R. D., Strong, D., Bryson, D. and Strganac, T., "Static Nonlinear Aeroelastic Analysis of a Blended Wing Body," *46th AIAA / ASME / ASCE / AHS / ASC Structures, Structural Dynamics, and Materials Conference*, Austin, TX, Apr. 18-21, 2005.

[16]Lockyer, A. J., Drake, A., Bartley-Cho, J., Vartio, E., Solomon, D. and Shimko, T., "High Lift over Drag Active (HiLDA) Wing," AFRL-VA-WP-TR-2005-3066, Apr., 2005.

[17]Livne, E. and Weisshaar, T. A., "Aeroelasticity of Nonconventional Airplane Configurations - Past and Future," *Journal of Aircraft*, Vol. 40, No. 6, 2003, pp. 1047-1065.

[18]Cesnik, C. E. S. and Brown, E. L., "Active Wing Warping Control of a Joined-Wing Airplane Configuration," *44th AIAA / ASME / ASCE / AHS / ASC Structures, Structural Dynamics, and Materials Conference*, Norfolk, VA, Apr. 7-10, 2003.

[19]Brown, E. L., "Integrated Strain Actuation In Aircraft With Highly Flexible Composite Wings," Ph.D. Dissertation, Department of Mechanical Engineering, Massachusetts Institute of Technology, Cambridge, MA, 2003.

[20]Shearer, C. M., "Coupled Nonlinear Flight Dynamics, Aeroelasticity, and Control of Very Flexible Aircraft," Ph.D. Dissertation, Department of Aerospace Engineering, The University of Michigan, Ann Arbor, MI, 2006.

[21]Su, W., "Coupled Nonlinear Aeroelasticity and Flight Dynamics of Fully Flexible Aircraft," Ph.D. Dissertation, Department of Aerospace Engineering, The University of Michigan, Ann Arbor, MI, 2008.

[22]Cesnik, C. E. S. and Su, W., "Nonlinear Aeroelastic Modeling and Analysis of Fully Flexible Aircraft," *46th AIAA / ASME / ASCE / AHS / ASC Structures, Structural Dynamics, and Materials Conference*, Austin, TX, Apr. 18-21, 2005.

[23]Peters, D. A. and Johnson, M. J., "Finite-State Airloads for Deformable Airfoils on Fixed and Rotating Wings," *Proceedings of Symposium on Aeroelasticity and Fluid/Structure Interaction/Proceedings of the Winter Annual Meeting*, Fairfield, NJ, 1994.